# SEARCH FOR TIME-INDEPENDENT NEUTRINO EMISSION FROM ASTROPHYSICAL SOURCES WITH 3 yr OF IceCube DATA

M. G. Aartsen[1], R. Abbasi[2], Y. Abdou[3], M. Ackermann[4], J. Adams[5], J. A. Aguilar[6], M. Ahlers[2], D. Altmann[7], J. Auffenberg[2], X. Bai[8,43], M. Baker[2], S. W. Barwick[9], V. Baum[10], R. Bay[11], J. J. Beatty[12,13], S. Bechet[14], J. Becker Tjus[15], K.-H. Becker[16], M. L. Benabderrahmane[4], S. BenZvi[2], P. Berghaus[4], D. Berley[17], E. Bernardini[4], A. Bernhard[18], D. Z. Besson[19], G. Binder[11,20], D. Bindig[16], M. Bissok[21], E. Blaufuss[17], J. Blumenthal[21], D. J. Boersma[22], S. Bohaichuk[23], C. Bohm[24], D. Bose[25], S. Böser[26], O. Botner[22], L. Brayeur[25], H.-P. Bretz[4], A. M. Brown[5], R. Bruijn[27], J. Brunner[4], M. Carson[3], J. Casey[28], M. Casier[25], D. Chirkin[2], A. Christov[6], B. Christy[17], K. Clark[29], F. Clevermann[30], S. Coenders[21], S. Cohen[27], D. F. Cowen[29,31], A. H. Cruz Silva[4], M. Danninger[24], J. Daughhetee[28], J. C. Davis[12], M. Day[2], C. De Clercq[25], S. De Ridder[3], P. Desiati[2], K. D. de Vries[25], M. de With[7], T. DeYoung[29], J. C. Díaz-Vélez[2], M. Dunkman[29], R. Eagan[29], B. Eberhardt[10], J. Eisch[2], S. Euler[21], P. A. Evenson[8], O. Fadiran[2], A. R. Fazely[32], A. Fedynitch[15], J. Feintzeig[2], T. Feusels[3], K. Filimonov[11], C. Finley[24], T. Fischer-Wasels[16], S. Flis[24], A. Franckowiak[26], K. Frantzen[30], T. Fuchs[30], T. K. Gaisser[8], J. Gallagher[33], L. Gerhardt[11,20], L. Gladstone[2], T. Glüsenkamp[4], A. Goldschmidt[20], G. Golup[25], J. G. Gonzalez[8], J. A. Goodman[17], D. Góra[4], D. T. Grandmont[23], D. Grant[23], A. Groß[18], C. Ha[11,20], A. Haj Ismail[3], P. Hallen[21], A. Hallgren[22], F. Halzen[2], K. Hanson[14], D. Heereman[14], D. Heinen[21], K. Helbing[16], R. Hellauer[17], S. Hickford[5], G. C. Hill[1], K. D. Hoffman[17], R. Hoffmann[16], A. Homeier[26], K. Hoshina[2], W. Huelsnitz[17,44], P. O. Hulth[24], K. Hultqvist[24], S. Hussain[8], A. Ishihara[34], E. Jacobi[4], J. Jacobsen[2], K. Jagielski[21], G. S. Japaridze[35], K. Jero[2], O. Jlelati[3], B. Kaminsky[4], A. Kappes[7], T. Karg[4], A. Karle[2], J. L. Kelley[2], J. Kiryluk[36], J. Kläs[16], S. R. Klein[11,20], J.-H. Köhne[30], G. Kohnen[37], H. Kolanoski[7], L. Köpke[10], C. Kopper[2], S. Kopper[16], D. J. Koskinen[29], M. Kowalski[26], M. Krasberg[2], K. Krings[21], G. Kroll[10], J. Kunnen[25], N. Kurahashi[2], T. Kuwabara[8], M. Labare[3], H. Landsman[2], M. J. Larson[38], M. Lesiak-Bzdak[36], M. Leuermann[21], J. Leute[18], J. Lünemann[10], O. Macías[5], J. Madsen[39], G. Maggi[25], R. Maruyama[2], K. Mase[34], H. S. Matis[20], F. McNally[2], K. Meagher[17], M. Merck[2], T. Meures[14], S. Miarecki[11,20], E. Middell[4], N. Milke[30], J. Miller[25], L. Mohrmann[4], T. Montaruli[6,45], R. Morse[2], R. Nahnhauer[4], U. Naumann[16], H. Niederhausen[36], S. C. Nowicki[23], D. R. Nygren[20], A. Obertacke[16], S. Odrowski[18], A. Olivas[17], A. Omairat[16], A. O'Murchadha[14], L. Paul[21], J. A. Pepper[38], C. Pérez de los Heros[22], C. Pfendner[12], D. Pieloth[30], E. Pinat[14], J. Posselt[16], P. B. Price[11], G. T. Przybylski[20], L. Rädel[21], M. Rameez[6], K. Rawlins[40], P. Redl[17], R. Reimann[21], E. Resconi[18], W. Rhode[30], M. Ribordy[27], M. Richman[17], B. Riedel[2], J. P. Rodrigues[2], C. Rott[41], T. Ruhe[30], B. Ruzybayev[8], D. Ryckbosch[3], S. M. Saba[15], T. Salameh[29], H.-G. Sander[10], M. Santander[2], S. Sarkar[42], K. Schatto[10], F. Scheriau[30], T. Schmidt[17], M. Schmitz[30], S. Schoenen[21], S. Schöneberg[15], A. Schönwald[4], A. Schukraft[21], L. Schulte[26], O. Schulz[18], D. Seckel[8], Y. Sestayo[18], S. Seunarine[39], R. Shanidze[4], C. Sheremata[23], M. W. E. Smith[29], D. Soldin[16], G. M. Spiczak[39], C. Spiering[4], M. Stamatikos[12,46], T. Stanev[8], A. Stasik[26], T. Stezelberger[20], R. G. Stokstad[20], A. Stößl[4], E. A. Strahler[25], R. Ström[22], G. W. Sullivan[17], H. Taavola[22], I. Taboada[28], A. Tamburro[8], A. Tepe[16], S. Ter-Antonyan[32], G. Tešić[29], S. Tilav[8], P. A. Toale[38], S. Toscano[2], E. Unger[15], M. Usner[26], S. Vallecorsa[6], N. van Eijndhoven[25], A. Van Overloop[3], J. van Santen[2], M. Vehring[21], M. Voge[26], M. Vraeghe[3], C. Walck[24], T. Waldenmaier[7], M. Wallraff[21], Ch. Weaver[2], M. Wellons[2], C. Wendt[2], S. Westerhoff[2], N. Whitehorn[2], K. Wiebe[10], C. H. Wiebusch[21], D. R. Williams[38], H. Wissing[17], M. Wolf[24], T. R. Wood[23], K. Woschnagg[11], D. L. Xu[38], X. W. Xu[32], J. P. Yanez[4], G. Yodh[9], S. Yoshida[34], P. Zarzhitsky[38], J. Ziemann[30], S. Zierke[21], and M. Zoll[24]

[1] School of Chemistry & Physics, University of Adelaide, Adelaide SA 5005, Australia
[2] Department of Physics and Wisconsin IceCube Particle Astrophysics Center, University of Wisconsin, Madison, WI 53706, USA
[3] Department of Physics and Astronomy, University of Gent, B-9000 Gent, Belgium
[4] DESY, D-15735 Zeuthen, Germany
[5] Department of Physics and Astronomy, University of Canterbury, Private Bag 4800, Christchurch, New Zealand
[6] Département de physique nucléaire et corpusculaire, Université de Genève, CH-1211 Genève, Switzerland
[7] Institut für Physik, Humboldt-Universität zu Berlin, D-12489 Berlin, Germany
[8] Bartol Research Institute and Department of Physics and Astronomy, University of Delaware, Newark, DE 19716, USA
[9] Department of Physics and Astronomy, University of California, Irvine, CA 92697, USA
[10] Institute of Physics, University of Mainz, Staudinger Weg 7, D-55099 Mainz, Germany
[11] Department of Physics, University of California, Berkeley, CA 94720, USA
[12] Department of Physics and Center for Cosmology and Astro-Particle Physics, Ohio State University, Columbus, OH 43210, USA
[13] Department of Astronomy, Ohio State University, Columbus, OH 43210, USA
[14] Université Libre de Bruxelles, Science Faculty CP230, B-1050 Brussels, Belgium
[15] Fakultät für Physik & Astronomie, Ruhr-Universität Bochum, D-44780 Bochum, Germany
[16] Department of Physics, University of Wuppertal, D-42119 Wuppertal, Germany
[17] Department of Physics, University of Maryland, College Park, MD 20742, USA
[18] T. U. Munich, D-85748 Garching, Germany
[19] Department of Physics and Astronomy, University of Kansas, Lawrence, KS 66045, USA
[20] Lawrence Berkeley National Laboratory, Berkeley, CA 94720, USA
[21] III. Physikalisches Institut, RWTH Aachen University, D-52056 Aachen, Germany
[22] Department of Physics and Astronomy, Uppsala University, Box 516, SE-75120 Uppsala, Sweden
[23] Department of Physics, University of Alberta, Edmonton, Alberta T6G 2E1, Canada
[24] Oskar Klein Centre and Department of Physics, Stockholm University, SE-10691 Stockholm, Sweden

$^{25}$ Vrije Universiteit Brussel, Dienst ELEM, B-1050 Brussels, Belgium
$^{26}$ Physikalisches Institut, Universität Bonn, Nussallee 12, D-53115 Bonn, Germany
$^{27}$ Laboratory for High Energy Physics, École Polytechnique Fédérale, CH-1015 Lausanne, Switzerland
$^{28}$ School of Physics and Center for Relativistic Astrophysics, Georgia Institute of Technology, Atlanta, GA 30332, USA
$^{29}$ Department of Physics, Pennsylvania State University, University Park, PA 16802, USA
$^{30}$ Department of Physics, TU Dortmund University, D-44221 Dortmund, Germany
$^{31}$ Department of Astronomy and Astrophysics, Pennsylvania State University, University Park, PA 16802, USA
$^{32}$ Department of Physics, Southern University, Baton Rouge, LA 70813, USA
$^{33}$ Department of Astronomy, University of Wisconsin, Madison, WI 53706, USA
$^{34}$ Department of Physics, Chiba University, Chiba 263-8522, Japan
$^{35}$ CTSPS, Clark-Atlanta University, Atlanta, GA 30314, USA
$^{36}$ Department of Physics and Astronomy, Stony Brook University, Stony Brook, NY 11794-3800, USA
$^{37}$ Université de Mons, 7000 Mons, Belgium
$^{38}$ Department of Physics and Astronomy, University of Alabama, Tuscaloosa, AL 35487, USA
$^{39}$ Department of Physics, University of Wisconsin, River Falls, WI 54022, USA
$^{40}$ Department of Physics and Astronomy, University of Alaska Anchorage, 3211 Providence Dr., Anchorage, AK 99508, USA
$^{41}$ Department of Physics, Sungkyunkwan University, Suwon 440-746, Korea
$^{42}$ Department of Physics, University of Oxford, 1 Keble Road, Oxford OX1 3NP, UK

## ABSTRACT

We present the results of a search for neutrino point sources using the IceCube data collected between 2008 April and 2011 May with three partially completed configurations of the detector: the 40-, 59-, and 79-string configurations. The live-time of this data set is 1040 days. An unbinned maximum likelihood ratio test was used to search for an excess of neutrinos above the atmospheric background at any given direction in the sky. By adding two more years of data with improved event selection and reconstruction techniques, the sensitivity was improved by a factor of 3.5 or more with respect to the previously published results obtained with the 40-string configuration of IceCube. We performed an all-sky survey and a dedicated search using a catalog of a priori selected objects observed by other telescopes. In both searches, the data are compatible with the background-only hypothesis. In the absence of evidence for a signal, we set upper limits on the flux of muon neutrinos. For an $E^{-2}$ neutrino spectrum, the observed limits are (0.9–5) $\times 10^{-12}$ TeV$^{-1}$ cm$^{-2}$ s$^{-1}$ for energies between 1 TeV and 1 PeV in the northern sky and (0.9–23.2) $\times 10^{-12}$ TeV$^{-1}$ cm$^{-2}$ s$^{-1}$ for energies between $10^2$ TeV and $10^2$ PeV in the southern sky. We also report upper limits for neutrino emission from groups of sources that were selected according to theoretical models or observational parameters and analyzed with a stacking approach. Some of the limits presented already reach the level necessary to quantitatively test current models of neutrino emission.

*Key words:* astroparticle physics – cosmic rays – neutrinos – telescopes

*Online-only material:* color figures

## 1. INTRODUCTION

The origin of cosmic rays (CRs) is an unresolved puzzle. The prevailing model of CR acceleration assumes that charged particles receive their very high energies via repeated scattering across strong astrophysical shocks, the so-called first-order Fermi acceleration. Candidate sources of Galactic CRs are supernova explosions and their remnant shocks, which may accelerate charged particles via diffuse shock acceleration up to the CR "knee" ($\sim 3 \times 10^{15}$ eV). At higher energies it is believed that powerful extragalactic sources, such as $\gamma$-ray bursts, active galactic nuclei, or starburst galaxies, can supply the necessary environment for diffusive shock acceleration of CRs. For recent reviews, see, e.g., Dermer & Powale [2013], Learned & Mannheim [2000], Becker [2008b], and Anchordoqui & Montaruli [2010].

The direct observation of the sources of CRs is difficult. Charged particles deflect and diffuse in Galactic and intergalactic magnetic fields and do not reveal the direction of the CR source, except possibly at ultrahigh energies. However, the origin of CRs might be revealed by the detection of secondary $\gamma$ rays and neutrinos that are produced via hadronic interactions of CRs with radiation and gas in the vicinity of the source. The emission is a result of meson (mostly pion) production and subsequent decay, such as $\pi^0 \to \gamma\gamma$ or $\pi^+ \to \mu^+\nu_\mu$ and $\mu^+ \to e^+\nu_e\bar{\nu}_\mu$. However, super-TeV $\gamma$ rays suffer from absorption, $\gamma\gamma_{\rm bg} \to e^+e^-$, in the interstellar and extragalactic background light and can be significantly attenuated over extragalactic distances. Moreover, there exist alternative leptonic models of $\gamma$-ray production that are not directly related to the acceleration of CRs.

Astrophysical neutrinos are hence a "smoking-gun" signal for the sources of CRs. Because they are electrically neutral and only weakly interacting particles, their propagation over cosmological distances is not affected by strong absorption or deflection. Hence, their detection will make it possible to unequivocally identify the position of CR sources and will also help to quantify their energetics. In this paper we present the latest results of the search for neutrino point sources with the IceCube neutrino observatory. The analysis was performed on the data collected from 2008 to 2011 and concerns searches for steady neutrino sources.

Section 2 describes the IceCube detector and the detection principle. The three data samples and the corresponding event

---

$^{43}$ Also at Physics Department, South Dakota School of Mines and Technology, Rapid City, SD 57701, USA.
$^{44}$ Also at Los Alamos National Laboratory, Los Alamos, NM 87545, USA.
$^{45}$ Also at Sezione INFN, Dipartimento di Fisica, I-70126 Bari, Italy.
$^{46}$ Also at NASA Goddard Space Flight Center, Greenbelt, MD 20771, USA.

selections are discussed in Section 3. The methodology used to combine data from different years and detector configurations in a point source search is given in Section 4, and Section 5 presents the results of the analysis, including a discussion of their impact on some recent astrophysical models of neutrino emission. The systematic uncertainties are described in Section 6, and conclusions are drawn in Section 7.

## 2. DETECTOR

The IceCube detector at the South Pole is designed to observe neutrinos of astrophysical origin and atmospheric muons and neutrinos induced by cosmic rays at the energies around and above the knee.

IceCube detects the Cherenkov light emitted by secondary leptons that are produced in charged- and neutral-current neutrino interactions with the matter surrounding the detector and is hence sensitive to all neutrino flavors. For neutrino point source searches we select events from charged-current interactions of muon neutrinos since they result in secondary muons with long tracks and a good directional reconstruction. Above TeV energies, the scattering angle between the muon and the incoming neutrino is smaller than the angular resolution of the detector. In order to detect the Cherenkov light, IceCube uses an array of 5160 digital optical modules (DOMs; Abbasi et al. 2010) deployed on 86 strings at a depth of 1.5–2.5 km below the surface just above the bedrock in the clear, deep ice. The DOMs are spherical, pressure-resistant glass housings containing a 25-cm-diameter Hamamatsu photomultiplier tube (PMT) and electronics for waveform digitization (Abbasi et al. 2009a). High-quantum-efficiency PMTs are used in a denser subarray located in the center of the detector. This subarray, called Deep-Core, enhances the sensitivity to low-energy neutrinos (Abbasi et al. 2012b). A surface CR detector, called IceTop, completes the IceCube Observatory (Abbasi et al. 2013b). It uses 324 PMTs to detect the electromagnetic component of air showers produced by CR interactions in the atmosphere.

The construction of the IceCube Observatory started in the Austral summer of 2004 and ended in 2010 December. Data acquisition with the complete configuration started in 2011 May. However, IceCube has been providing physics results since the completion of the nine-string array in 2006. From 2008 April to 2011 May three different configurations of the IceCube detector were in operation. Figure 1 shows the positions of the strings in the 40-string configuration (IC-40), which took data from 2008 April 5 to 2009 May 20, the 59-string configuration (IC-59) active from 2009 May 20 to 2010 May 31, and the 79-string configuration (IC-79) active from 2010 May 31 to 2011 May 13. Figure 1 also shows the final 86-string IceCube configuration. The total live-time over the entire period used in this work corresponds to 1040 days collected with the IC-40, IC-59, and IC-79 configurations, and the average uptime is 92% at final analysis level.

In this analysis we used a simple multiplicity trigger where eight or more DOMs recorded a light deposition within a 5 $\mu$s time window (SMT8). Most of the events that are selected by this trigger are composed of muons produced by CR in the atmosphere above the detector (about 2.2 kHz at trigger level in the 79-string configuration). These events enter the detector only from above since muons produced in the opposite hemisphere of the atmosphere are absorbed by the Earth. Only about 1 in $10^6$ recorded events is induced by an atmospheric neutrino, which can reach IceCube from any direction. The goal of all further event selections is to increase the ratio of
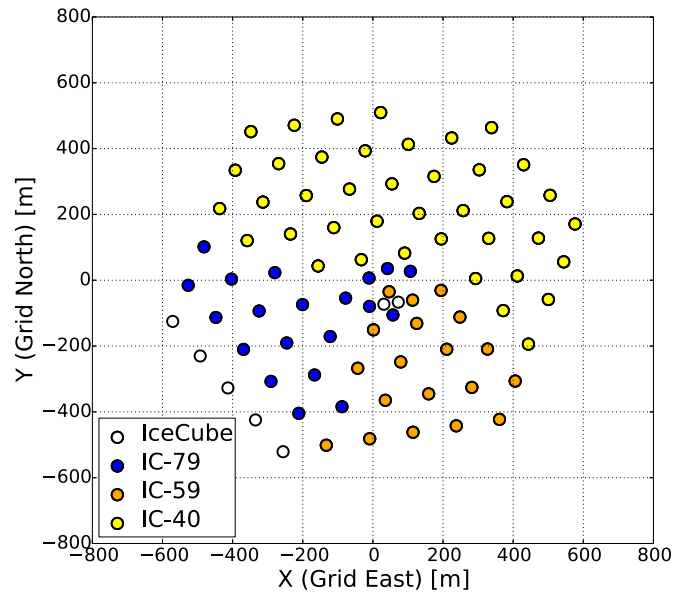


**Figure 1.** Detector layout in the IceCube coordinate system. The grid north axis is aligned with the prime meridian, pointing toward Greenwich, UK. The grid east axis points 90° clockwise from grid north. The circles represent the surface string positions corresponding to the final geometry of the whole IceCube detector. The IC-40 configuration is represented by yellow dots. The orange circles represent the additional strings that form the IC-59 configuration. The IC-59 configuration together with the strings indicated by blue circles represent the IC-79 configuration. The empty circles are the strings added for the complete detector.

(A color version of this figure is available in the online journal.)

the neutrino signal from astrophysical sources with respect to the muon background. The key elements of the selection of the neutrino candidates are reconstructions of the event direction and of the deposited energy. Only high-quality reconstructed events are selected in order to strongly reduce the background of downward-going muons that are misreconstructed as upward going. Moreover, since in many signal scenarios the signal is expected to have higher energy than the atmospheric background, the estimated energy can be used to suppress the low-energy muon background. For instance, the first-order Fermi acceleration mechanisms in supernova remnant (SNR) shocks predict a neutrino power law spectrum of $E^{-2}$ (Bell 1978; Schlickeiser 1989), while the atmospheric neutrinos have a differential spectrum in energy above 100 GeV that goes as $E^{-3.7}$ (Abbasi et al. 2011a).

A significant part of the background reduction is performed online at the South Pole (L1 filter), where first cuts on the quality of the reconstruction of up-going events from the Northern Hemisphere are applied and high-energy down-going muons from the Southern Hemisphere are selected. This filtering of events is designed to serve a large variety of different muon neutrino searches by maintaining a high signal efficiency. This reduction of atmospheric muon background is sufficient to send the remaining data off site by satellite, where they undergo further processing (L2 filter). Figure 2 shows the data rate of each run as a function of the modified Julian date for one of the data streams of the L2 filter, the muon filter. Also shown is the South Pole atmospheric temperature. Cosmic rays entering the Earth's atmosphere generate a hadronic cascade in which mesons, primarily pions and kaons, are produced. The atmospheric muon flux depends on the relative probability of decay or the interaction of these pions and kaons, which in turn depends on the local density of the atmosphere and therefore on
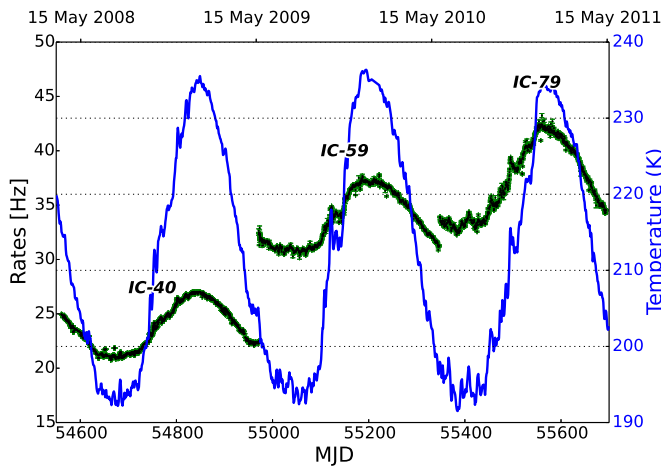
**Figure 2.** IceCube event rates for the three periods at the muon filter level as a function of the modified Julian date (MJD). The correlation with the effective temperature of the South Pole atmosphere is also shown. The effective temperature is the convolution of the atmospheric temperature profile with the inclusive muon production spectrum (Desiati et al. 2011). Note that the $y$ axes are shown with offsets for better visibility.

(A color version of this figure is available in the online journal.)

the atmospheric temperature. Figure 2 shows how the seasonal modulations of the temperature are strongly correlated with the atmospheric muon rate.

Most track reconstructions performed at the South Pole are likelihood based, with the exception of *linefit*, which is an algorithm used as a seed for more precise and CPU-intense reconstructions to follow. These likelihood-based fits use the photon arrival time distribution for track reconstruction (Ahrens et al. 2004). The multiphotoelectron likelihood function, which uses time and amplitude information of the PMT pulses, is applied after several iterations of the single-photoelectron likelihood fit that uses only the pulse leading edge time. The energy estimation is performed after the track reconstruction since the muon direction information is used by the energy reconstruction algorithm. The muon energy proxy described in Abbasi et al. (2011b) was used in all 3 yr of data of this analysis together with a more recently developed algorithm described in Abbasi et al. (2013d) as an alternative energy estimator for the data collected with the 79-string configuration.

## 3. EVENT SELECTION

The first-order background rejection of the online filter is not sufficient for high-level data analyses. Up-going, high-energy neutrino candidates can be selected from the data by rejecting events with a poor reconstruction since they are more likely to be down-going muons by removing misreconstructed events with multiple muon tracks and by suppressing events with low energies. In the southern sky, it is not possible to reject the muon background on the basis of the reconstruction quality of the events, and the most energetic events are selected instead to improve the ratio of signal to background events (Abbasi et al. 2009b, 2011b). Reflecting the different detector geometries and the general improvement in the muon track reconstruction and identification of muon background events, we used a different event selection for each of the three periods of data used in this work.

The ability to observe a neutrino point source depends on the expected number of background events, the observable number

of neutrinos for a given source strength, the energies of these events, and the angular resolution. The discovery potential, defined as the flux needed to make a $5\sigma$ discovery in 50% of an ensemble of pseudoexperiments with a simulated signal of this strength, captures all these aspects and was used as the main figure of merit to optimize the event selections. Diffuse shock acceleration leads to power law spectra with a spectral index around 2 (Bell 1978; Schlickeiser 1989), and neutrinos originating in CR interactions near the source are expected to follow a similar spectrum. We thus used an $E^{-2}$ spectrum as our main benchmark model. Several Galactic $\gamma$-ray sources have energy spectra with energy cutoffs at a few TeV (Mandelartz & Becker Tjus 2013), supporting the idea that Galactic neutrino spectra may present cutoff spectra as well (Kistler & Beacom 2006; Vissani 2006). We therefore also took softer neutrino spectra into account. These softer spectra were modeled by larger spectral indexes (e.g., 2.7 or 3) and/or by exponential energy cutoffs.

### 3.1. IceCube 40-String Data Sample

During the IC-40 period, IceCube recorded data more than 99% of the time, and 92% of the data were used after selecting periods of stable detector operation. The data used after this selection correspond to a live-time of 375.5 days. The event selection for the point source analysis of the IC-40 data was obtained by cuts on a number of well understood and powerful variables and is described in detail in Abbasi et al. (2011b). In the southern sky, events were selected with a cut on the reconstructed energy of the event, which was parameterized as a function of the reconstructed declination. The final sample of events obtained from the IC-40 configuration contained a total of 36,900 events: 14,121 from the northern sky and 22,779 from the southern sky.

### 3.2. IceCube 59-String Data Sample

The data from the IC-59 configuration correspond to a live-time of 348.1 days. The rate of the SMT8 trigger was of the order of 1.5 kHz, and the online muon filter rate was a factor two higher than in the previous configuration, as can be seen in Figure 2.

It was shown in Abbasi et al. (2013a) and Abbasi et al. (2012a) that a higher efficiency for up-going neutrino events with energies below 10 TeV can be achieved with multivariate approaches without compromising the discovery potential for neutrino sources with hard energy spectra. In the IC-59 data sample, we used boosted decision trees (BDTs; Kerthi et al. 2001) to this end. BDTs are widely used in two-class classification problems where a larger set of weakly discriminating variables is available (Hastie et al. 2009) and are thus well suited for the selection of neutrino events from the IceCube data.

The multivariate cuts were based on 12 observables with a high discriminating power between signal and background. We used 10% of the atmospheric muon-dominated data as a background model for the BDT training. Any possible astrophysical signal contributes only a very small fraction to the data at this level. The observables were selected such that their correlation in the background-dominated data sample was below 50%. The signal was modeled with a Monte Carlo simulation. Two different signal energy spectra were considered: an $E^{-2}$ spectrum and one with a neutrino spectrum of $E^{-2.7}$ to account for softer neutrino spectra. Additionally, the reconstructed track was
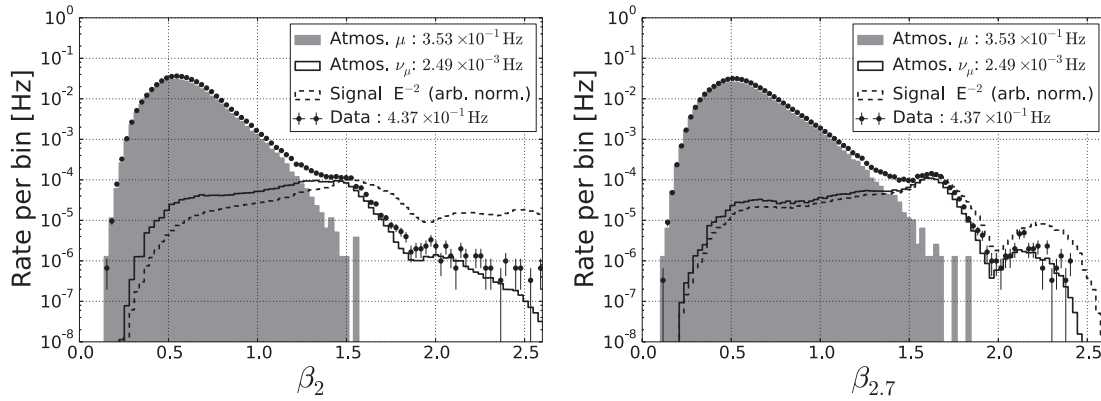
**Figure 3.** Distribution of the BDT score for the ensemble of trees trained with (left) an $E^{-2}$ spectrum and (right) an $E^{-2.7}$ spectrum as the signal. The data shown here are from the IC-59 configuration, and examples for a signal distribution are shown with an arbitrary normalization.

required to be within $0°5$ of the simulated direction in order to train the BDT with only well-reconstructed events.

For computational reasons, the observables were split in two sets of eight and four variables, and a BDT was defined for each set separately. The final selection was based on a combination of the two BDT scores. Figure 3 shows the distribution of the combined BDT scores obtained by the training with the two different signal spectra for data and a simulated neutrino signal as well as for the simulated atmospheric muon and neutrino backgrounds.

Events in the Southern Hemisphere were selected with a cut on the reconstructed energy. The strength of the cut was varied as a function of the declination. In addition, we used the veto capability of the surface array IceTop (Auffenberg et al. 2011) to reduce the muon background. Atmospheric muons are accompanied by extended air showers, which can produce early hits in the IceTop surface array. The veto is defined by counting the number of detected photo electrons in IceTop within a time window around the expected arrival time of the shower front in the surface detector. In the IC-59 event selection, the IceTop veto was used for events with reconstructed declinations between $-90°$ and $-40°$. The best veto efficiency is expected for events with high energies, heavy primaries, vertical directions, and a shower axis close to the IceTop detector. Figure 4 shows the veto capability of the IceTop surface array using atmospheric muon-dominated data from IC-79. The IceTop veto allows us to reject the background with 99% efficiency in the vertically down-going region without losing signal neutrino efficiency ($\lesssim 1\%$).

The final data sample for the IC-59 configuration has a total number of 107,569 events, among which almost two-thirds come from the southern sky. The rest are neutrino candidates in the northern sky.

### 3.3. IceCube 79-String Data Sample

As illustrated in Figure 1, the IC-79 configuration almost had the final volume of the full IceCube detector. With the largest detector size among the configurations discussed here, the background from coincidences of two or more atmospheric muons within the same readout window is more abundant than in the previous ones. At the same time, the number of neutrino events in coincidence with an atmospheric down-going muon increased as well. We applied a topological hit clustering based on the spatial and temporal separation of recorded PMT signals to separate neutrinos from coincident muons. In addition to the reconstruction of the full event, we applied the same
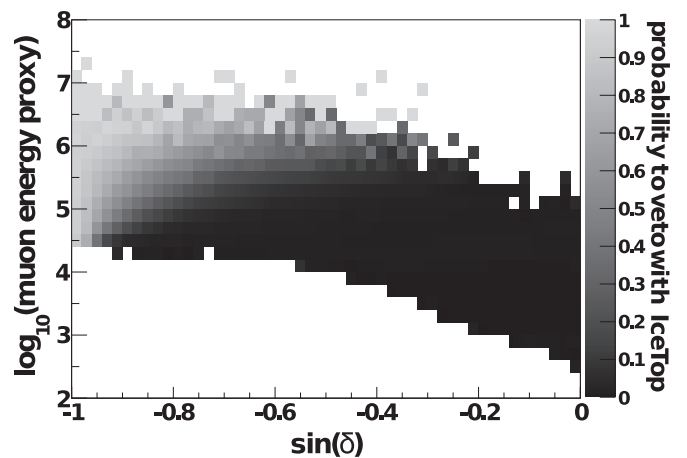


**Figure 4.** IceTop veto capability as a function of the sine of the declination $\delta$ of the detected muon and the estimated energy of the detected muon in the detector based on the data from IC-79. The events used for this visualization passed an intermediate set of event selection criteria but are still dominated by atmospheric muons. Events with three or more veto hits within a time window of $\pm 1000$ ns around the expected shower front arrival time are rejected. Ten percent of the experimental data were used for this plot, and the white areas correspond to regions where no event was observed.

reconstruction to up to three topologically connected subsets of hits. Among these and the original reconstructed track, only the most likely neutrino candidate was selected. If only the reconstruction of the full hit information passed the cuts but none of the subsets did, the events were rejected to improve the background suppression. A visual inspection of more than 50 events at the final selection level showed that the topological splitting of events allowed us to select additional high-quality neutrino events from which a coincident muon contamination was removed.

Two different high-level event selections have been developed, which we denote sample A and sample B in the following. While all the results presented in this article have been obtained on sample A, we used sample B for cross-checks and validation of the point source analysis.

For both event samples, we used a combination of BDTs for the event selection in the northern sky and divided this area into two regions, a horizontal one and a vertical one. For sample A (B), we considered events within $-5° \leqslant \delta \leqslant +40°$ ($0° \leqslant \delta \leqslant +35°$) and events within $+40° \leqslant \delta \leqslant +90°$ ($+35° \leqslant \delta \leqslant +90°$) separately. The two bands are characterized by different expected signal energy spectra because of the
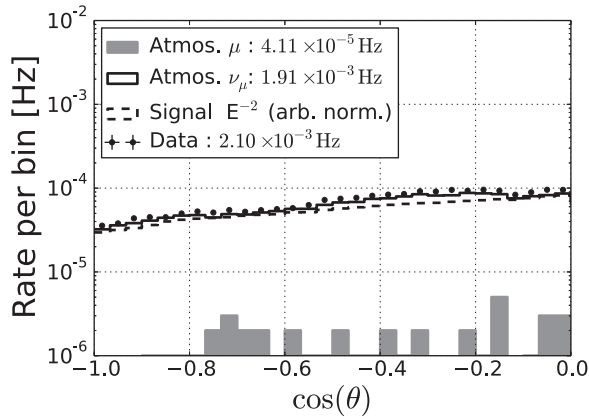
**Figure 5.** Zenith distribution at the final cut level for the up-going neutrino selection. Points represent data. The dashed line is a benchmark $E^{-2}$ astrophysical neutrino signal normalized to the all-sky atmospheric neutrino rate shown to illustrate how a hypothetical signal distributes in zenith. The solid line is the simulated atmospheric neutrino contribution, and the filled histogram shows the simulated contribution of misreconstructed atmospheric muons after all cuts estimated.



**Figure 6.** Discovery potential for point sources at the $5\sigma$ confidence level for an $E^{-2}$ spectrum as a function of declination for the 3 yr of IceCube data when sample A (dashed) or sample B (solid) is used for the IC-79 data.

absorption of high-energy neutrinos in the Earth and by different distributions of the background.

For sample A, 17 observables were selected for the BDT on the basis of their discrimination power between a neutrino signal and the muon background. They were split into two sets of nine and eight variables each. In addition, we asked for the background and signal correlation coefficients between any two variables in the same set to be below 50%. A number of variables with less discrimination power were included since BDTs are robust against the inclusion of weak variables. The final cut parameter was defined by a combination of the two BDT scores for each zenith angle region.

In sample B, only highly discriminating variables were included in the BDTs, and the event selection used a different number of variables in the horizontal region where the signal is dominated by higher-energy events. Nine variables were selected for the vertical region, and 15 variables were chosen for the horizontal region. No requirement was applied to limit the correlations between the variables, allowing us to use all selected variables in a single BDT in each region. Eight of the observables used for the BDT of sample B were also used in sample A.

As in the IC-59 selection we trained the BDTs with two different signal spectra, using again the $E^{-2}$ spectrum as a benchmark for hard spectra. As representative of a soft spectrum, we used an $E^{-2.4}$ spectrum with a cutoff at 7 TeV for sample A and an $E^{-2.7}$ spectrum for sample B.

The final selections were optimized to provide the best discovery potential for $E^{-2}$ neutrino fluxes. At the same time, we aimed to achieve a near-optimal discovery potential for softer spectra by adding additional lower-energy events. We also took special care in having a smooth transition in the event rate between the two declination regions. Since IceCube is located at the South Pole, the zenith angle $\theta$ and declination angle $\delta$ are simply related as $\theta = \delta + 90°$. Figure 5 shows the zenith distribution for the up-going (northern sky) event selection in sample A. As can be seen, it is fully dominated by atmospheric neutrinos, and only a small fraction of misreconstructed downgoing atmospheric muons survive after the event selection.

For sample A, we extended the cuts from the up-going region to the Southern Hemisphere by using the same set of cuts and a
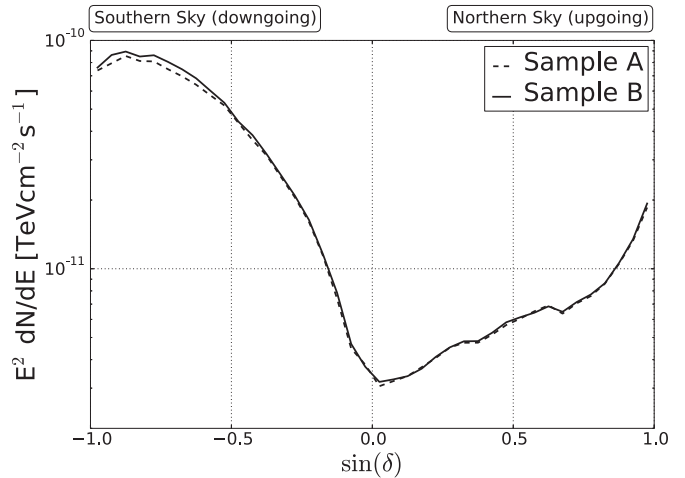
retrained BDT as an intermediate event selection. In addition, an angular uncertainty estimator was required to be smaller than $2°$. We also applied a veto by rejecting events with three or more veto hits in the surface array IceTop. The probability to veto events by accidental coincidences was estimated by using experimental data from an off-time window where no correlated signal in IceTop is expected. It is below 1% at every declination and energy. The probability to veto a background event is shown in Figure 4. The background rejection power is above 90% for high-energy, vertical down-going muons. To further decrease the rate of accidental coincidences, we applied the IceTop veto cut only in those regions of the energy-declination space where it is most efficient. In this way, the accidental veto probability is much smaller than 1%, and its effect on the signal efficiency can be neglected. The effect of the IceTop veto in the IC-79 and IC-59 event selection is visible in Figure 6. For very vertically down-going events ($\sin\delta < -0.85$), where the veto is most efficient, there is a decrease in the discovery flux. Finally, a declination-dependent energy cut was used to select a constant number of events per solid angle and to provide a smooth transition from the Northern to the Southern Hemisphere.

For sample B, a simple energy cut depending on the declination was applied to select a constant number of events per solid angle. The same soft IceTop veto as above was used to reject part of the down-going atmospheric muon background at the very vertical zenith angles. A study performed on this sample indicated that no significant gain in the discovery potential could be achieved by selecting a larger number of events in the Southern Hemisphere.

Sample A contains 109,866 events, of which 50,857 come from the northern sky and 59,009 are located in the southern sky.

The two samples yield the same discovery potential for steady, pointlike neutrino sources both for hard (represented by an $E^{-2}$ neutrino signal spectrum) and soft (represented by an $E^{-3}$ neutrino signal spectrum) neutrino spectra at every declination (see Figure 6). The differences are smaller than the statistical uncertainty of the estimation. This is a confirmation of the validity of the independent BDT selections.

Sample B has a slightly larger effective area for events at lower energies than sample A at the cost of a higher muon contamination in the Northern Hemisphere. Considering events
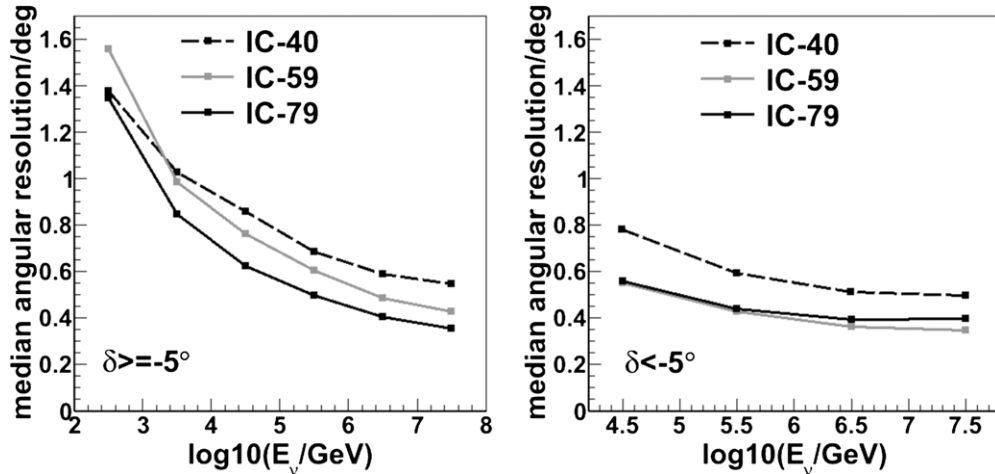
**Figure 7.** Neutrino angular resolution defined as the median of the point-spread function of the true neutrino direction and the reconstructed muon direction for (right) the northern and (left) the southern sky at analysis level.

with reconstructed declinations above $0°$, we observe that the events that are contained in both samples make up 75% of the events in sample A and 67% of the events in sample B. The difference in the percentages reflects the smaller number of events in sample A. The overlap between the two samples is larger for events with small angular uncertainties, increasing to 81% of the events in sample A and 90% of sample B being contained in both samples if events with angular uncertainty estimates smaller than $0°.5$ are considered. Thus, the probability for a more signal-like, well-reconstructed event to be in both samples is higher than the corresponding probability for an event with a poor reconstruction. A visual inspection of the hit patterns of a subset of the events confirms that the contribution of background events from atmospheric muons is smaller in the group of events that is in both samples. In particular, we have visually checked the hit patterns of more than 100 up-going events that are in both samples and have an angular uncertainty estimate smaller than $0°.5$; all of these were well-reconstructed up-going, i.e., neutrino-induced, events.

The overlap of the two event samples in the southern sky is much smaller than in the northern sky. In the region from declination $-90°$ to $0°$, we observed that 38% of the events in sample A are also contained in sample B and that 27% of the events in sample B are also in sample A. The fraction of events common in both samples increases for smaller angular uncertainty estimates. The smaller overlap is expected. The event selection in sample A disfavors events with very large energy losses with respect to the event selection in sample B. Moreover, both event selections apply a filtering of different strengths before the energy cut is applied on the steeply falling spectrum. Moving the strength of the energy cut at any declination by a small amount will decrease the overlap between two event selections significantly.

Table 1 summarizes the live-time, the estimated rate of atmospheric neutrinos, and the number of up-going and down-going track events in the three different configurations using sample A for the IC-79 configuration. The total number of events used in this analysis is 108,317 up-going events, of which the majority are atmospheric neutrinos, and 146,018 down-going events, which are mostly from atmospheric muons.

Figure 7 shows the neutrino angular resolution in each of the three data samples. In the northern sky, the best angular resolution is observed in IC-79. The lowest-energy bin in the

**Table 1**
Summary of the Three Different IceCube Configurations Used in This Analysis

| Configuration | Live-time (days) | Atm. $\nu$s | # Up-going | # Down-going |
|---|---|---|---|---|
| IC-40 | 376 | 40/day | 14,121 | 22,779 |
| IC-59 | 348 | 120/day | 43,339 | 64,230 |
| IC-79 | 316 | 180/day | 50,857 | 59,009 |

**Notes.** We show the expected atmospheric neutrino rate from MC simulation weighted by the model in (Honda et al. 2007) and the numbers of up- and down-going events at final selection level. The numbers for the IC-79 are from sample A.

IC-40 sample has a better resolution than in the IC-59 sample because of the stricter event filtering applied in this energy range. The southern sky selection of the IC-59 sample applies stronger cuts than the IC-79 selection, leading to a slightly better angular resolution in this range.

The effective area $A_{\mathrm{eff}}^{\nu}$ for fluxes of $\nu_\mu + \bar{\nu}_\mu$ is shown in Figure 8 (left) for the three final event selections of IceCube and for the northern and southern skies.[47] Upward-going neutrinos must travel through the Earth and therefore can be absorbed, which explains the crossing at energies of $\sim 10^6$ GeV between the northern sky and southern sky effective areas. Compared to current imaging atmospheric Cerenkov telescopes such as H.E.S.S., the IceCube neutrino effective area is a factor of $\sim 4$ smaller than the corresponding $\gamma$-ray effective area at energies of 10 TeV (Masbou et al. 2009). For the tabulated data of this figure, see the Appendix.

Figure 8 (right) shows the declination-dependent central energy interval containing 90% of the events for three power law neutrino spectra of $E^{-2}$, $E^{-2.4}$, and $E^{-1.5}$ using the combination of the three different detector geometries. The energy response of the detector is very different in the southern sky (down-going events) compared to the northern sky (up-going events); this is partly due to the tight event selection in the southern sky and also due to the fact that Earth acts as target material for the up-going low-energy events, while in the southern sky only very high energy neutrinos will interact in the atmosphere and produce a signal in the detector. This effect is also clearly visible

---

[47] In neutrino Cerenkov detectors no distinction between $\nu_\mu$ and $\bar{\nu}_\mu$ can be made, and therefore, effective areas are usually given for fluxes of the sum of $\nu_\mu + \bar{\nu}_\mu$.
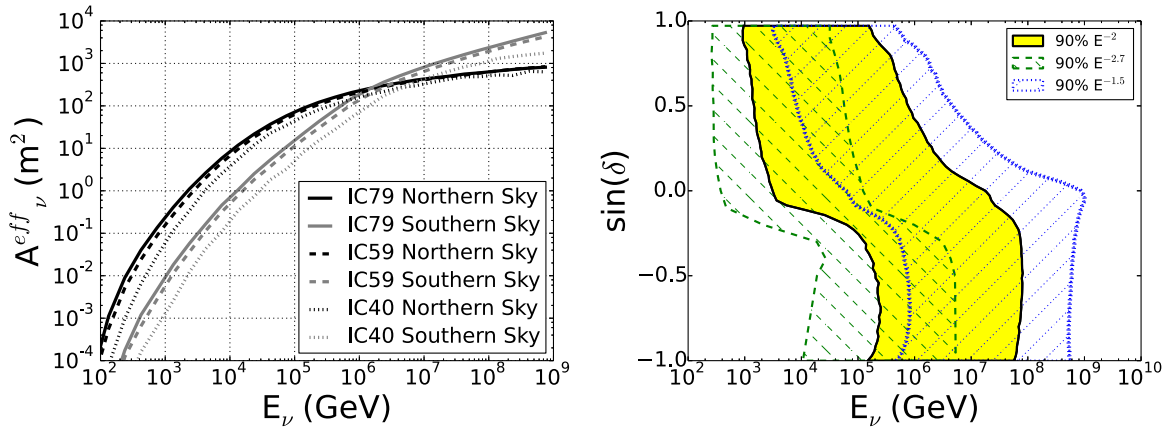
**Figure 8.** Left: solid-angle-averaged effective area for a mixed flux of an equal number of neutrinos and antineutrinos for the three event selections corresponding to three IceCube configurations for both the northern and southern skies. Right: the 90% central signal containment region for three different power law neutrino spectra as a function of declination for the three configurations combined.

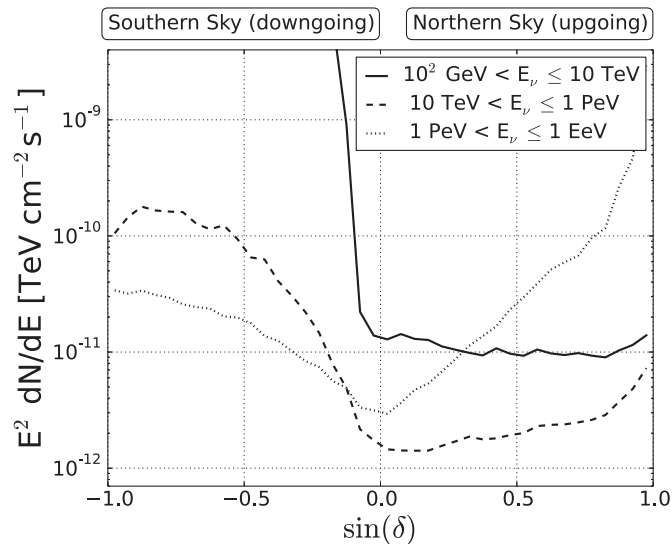(A color version of this figure is available in the online journal.)



**Figure 9.** Sensitivity for muon neutrino flux for an $E^{-2}$ spectrum for a 90% C.L. as a function of declination combining the 3 yr of data averaged over right ascension. The three different lines indicate three different energy ranges.

in the sensitivity for point sources of neutrinos as a function of declination shown in Figure 9. The dashed line in Figure 9 represents the expected sensitivity at the 90% confidence level (C.L.) as a function of declination for an $E^{-2}$ signal in the energy range between 10 TeV and 1 PeV, where most of the signal deposition is expected for this spectrum in the northern sky (see Figure 8, right). For this energy range, the sensitivity is best in the northern sky. The dotted and solid lines show the sensitivity for an $E^{-2}$ in a higher- and lower-energy range, respectively. In the higher-energy range, the sensitivity becomes more symmetrical around the horizon, where IceCube has its best sensitivity for high-energy events. On the other hand, for low-energy neutrinos ($E \leqslant 10$ TeV), IceCube sensitivity is mostly restricted to the northern sky.

## 4. THE LIKELIHOOD SEARCH METHOD

The goal of the search for neutrino point sources is to identify in the data a clustering of events in a particular direction of the sky that cannot be mimicked by the atmospheric muon

and neutrino background and is therefore incompatible with the background-only hypothesis. To this end, in IceCube we use an unbinned maximum likelihood ratio test. This method follows the one described in Braun et al. (2010) and is extended to combine different detector geometries. It calculates the significance of an excess of neutrinos over the atmospheric background by using both the directional information of the events and the energy to separate hard-spectrum signals from the softer spectra of atmospheric neutrinos and muons. The method models the expected neutrino signal from a point source in the sky using simulation, and since this search is background dominated, its estimate is done using real data.

The signal and background probability density functions (PDFs) are functions of the reconstructed declination and the reconstructed muon energy.

For a data sample of $N$ total events the PDF of the $i$th event in the $j$th sample (in our case the IC-40, IC-59, or IC-79 data set) with reconstructed energy $E_i$ located at an angular distance to the source of $|\boldsymbol{x}_i - \boldsymbol{x}_s|$ is given by

$$P_i^j\left(|\boldsymbol{x}_i - \boldsymbol{x}_s|, E_i, \gamma, n_s^j\right) = \frac{n_s^j}{N^j}\mathcal{S}_i^j + \left(1 - \frac{n_s^j}{N^j}\right)\mathcal{B}_i^j, \qquad (1)$$

where $\mathcal{S}_i^j$ and $\mathcal{B}_i^j$ are the signal and background PDF, respectively, and $n_s^j$ is the fraction of total number of signal events $n_s$ that is expected from the corresponding $j$th sample.

For time-integrated searches the signal PDF $\mathcal{S}_i^j$ is given by

$$\mathcal{S}_i^j = S_i^j(|\boldsymbol{x}_i - \boldsymbol{x}_s|, \sigma_i)\mathcal{E}_i^j(E_i, \delta_i, \gamma), \qquad (2)$$

where $S_i^j$ is the space contribution and depends on the angular uncertainty of the event $\sigma_i$ and the angular difference between the reconstructed direction of the event and the source. We model this probability as a two-dimensional Gaussian,

$$S_i^j = \frac{1}{2\pi\sigma_i^2}e^{-\frac{|\boldsymbol{x}_i - \boldsymbol{x}_s|^2}{2\sigma_i^2}}. \qquad (3)$$

The energy PDF $\mathcal{E}_i^j$ in the case of signal is a function of the reconstructed energy proxy $E_i$ and the spectral index $\gamma$ of a power law spectrum for a given declination (see Figure 10).
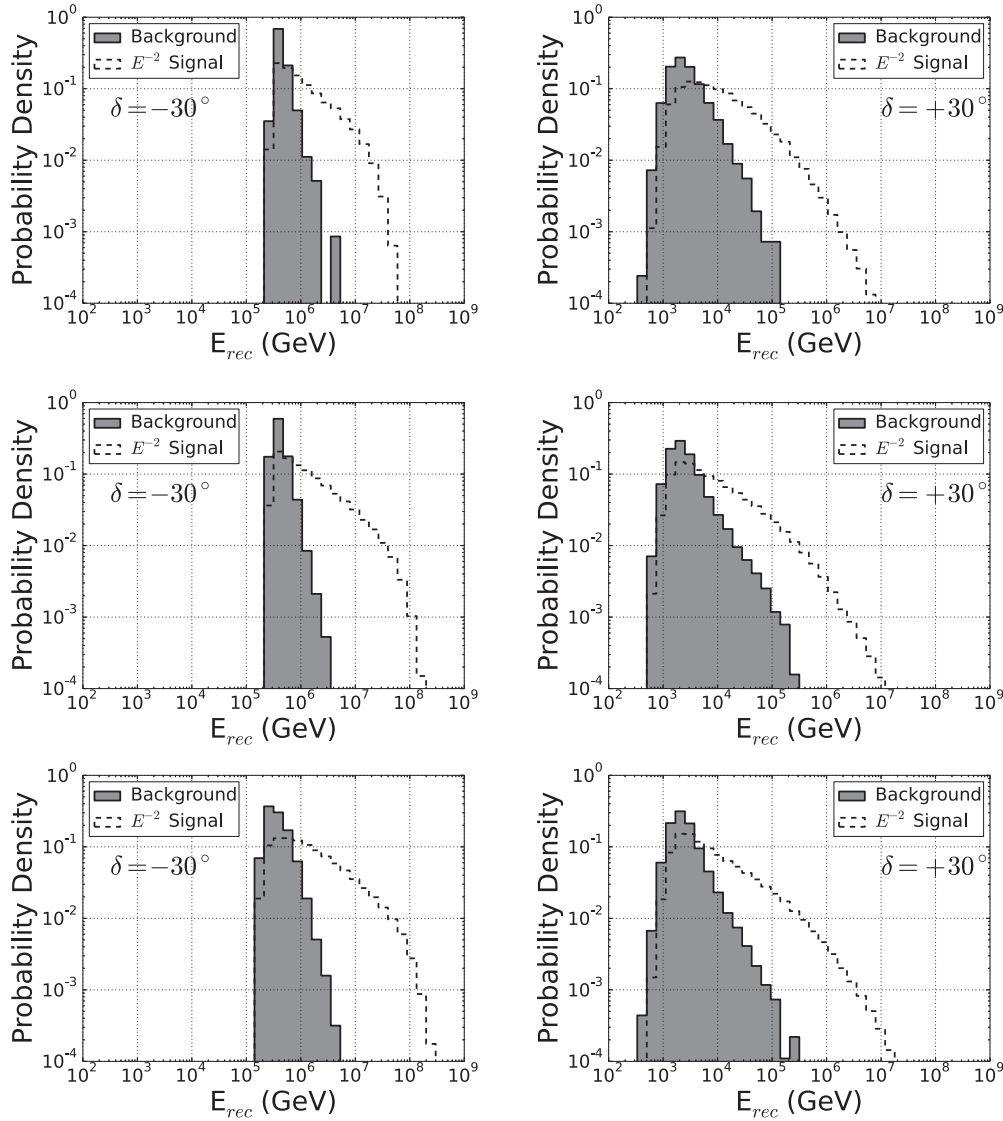
**Figure 10.** Probability density for the reconstructed muon energy for two different declinations, $\delta = -30°$ (left column) and $\delta = +30°$ (right column), for the background and an exemplary signal of an $E^{-2}$ spectrum for the three different detector configurations, the 40-string configuration (top row), the 59-string configuration (middle row), and the 79-string configuration (bottom row).

The background PDF $\mathcal{B}_i^j$ is obtained from the experimental data and is given by

$$\mathcal{B}_i^j = B_i^j(\delta_i)\mathcal{E}_i^j(E_i, \delta_i). \qquad (4)$$

The space term $B_i^j(\delta_i)$ is the event density per unit solid angle as a function of the declination. The background density is right ascension independent because of the Earth's rotation. The energy PDF for background $\mathcal{E}_i^j$ represents the probability of obtaining an energy $E_i$ from atmospheric backgrounds (neutrinos and muons) and therefore depends only on the declination.

The signal is considered to have the same spectrum for all data sets, and therefore, the spectral index meets the condition of $\gamma_j = \gamma$. The fitted numbers of signal events $n_s^j$ in each sample are also fixed relative to each other, according to the signal hypothesis tested and the fraction of signal events expected in each sample $f^j(\gamma, \delta)$. Simulation is used to calculate this fraction for a given spectral index, so that $n_s^j = f^j n_s$ (see Figure 11). In this way the likelihood $\mathcal{L}$ remains a function of

only the global parameters $n_s$ and $\gamma$ with respect to which it is maximized:

$$\mathcal{L}(\gamma, n_s) = \prod_j \mathcal{L}^j(\gamma, n_s^j) = \prod_j \prod_{i \in j} \left[ \frac{n_s^j}{N^j}\mathcal{S}_i^j + \left(1 - \frac{n_s^j}{N^j}\right)\mathcal{B}_i^j \right],$$
$$(5)$$

where $i \in j$ indicates that the $i$th event is in sample $j$. The test statistic (TS) is calculated from the likelihood ratio of the background-only (null) hypothesis over the best fitted signal-plus-background hypothesis:

$$\text{TS} = -2\log\left[\frac{\mathcal{L}(n_s = 0)}{\mathcal{L}(\hat{n}_s, \hat{\gamma})}\right]. \qquad (6)$$

Here $\hat{n}_s$ is the best fit number of source events, and $\hat{\gamma}$ is the best fit spectral index. In principle, $n_s$ may be positive or negative since both positive and negative fluctuations with respect to the background expectation may be observed. In the likelihood maximization, however, it is constrained to nonnegative values. Pseudoexperiments on randomized data
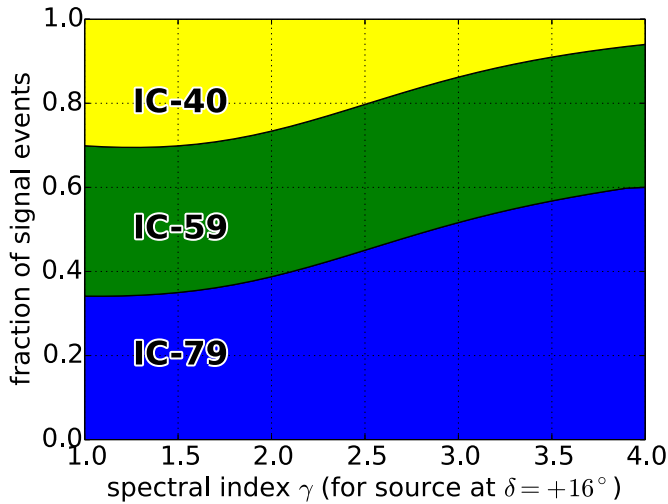
**Figure 11.** For a point source emitting a steady $E^{-\gamma}$ power law flux of neutrinos, as a function of $\gamma$, the fraction of the total signal events (at final cut level) that would be expected in each of the three data samples is shown. In this example (at source declination $\delta = +16°$), a signal from a very hard spectrum $E^{-1}$ source can be seen to be nearly evenly divided across the three seasons of data taking. A soft-spectrum $E^{-4}$ source, on the other hand, will result in most of the signal events being in the IC-59 and IC-79 data samples because of the larger geometric size and improved event selection at low energies. The relative efficiency of the three data-taking periods depends on the source declination as well as spectral index and is needed in the likelihood analysis to relate different numbers of signal events in different data samples to a common source flux normalization, depending on the tested index $\gamma$.

(A color version of this figure is available in the online journal.)

are performed to determine the significance of the observation. The randomization is achieved by the assignment of a random right ascension to each event in the data sample while all other event properties, such as the energy and declination, are left unchanged. The fraction of the pseudoexperiments that yield a TS value above the observed TS is quoted as the $p$-value of the observation.

For the stacking searches we used the method described in Achterberg et al. (2006) and Abbasi et al. (2011b). The signal PDF is modified by breaking it into a sum over $M$ sources. For one single sample the PDF can be rewritten as

$$
\begin{aligned}
\mathcal{S}_i \to \mathcal{S}_i^{\text{tot}} = \\
\frac{\sum_{k=1}^{M} W^k R^k(\gamma, \delta_k) \mathcal{S}_i^k(|\boldsymbol{x}_i - \boldsymbol{x}_k|, \sigma_i) \mathcal{E}_i(E_i, \delta_i, \gamma)}{\sum_{k=1}^{M} W^k R^k(\gamma, \delta_k)},
\end{aligned} \quad (7)
$$

where $W^k$ is the relative theoretical weight for the $k$th source in the catalog and $R^k(\gamma, \delta_k)$ is the detector acceptance for a flux with spectral index $\gamma$ at the coordinates $\boldsymbol{x}_k$. The theoretical weights are chosen to minimize the flux required for discovery for a possible signal hypothesis. In catalogs where the predicted neutrino luminosity is strongly correlated with $\gamma$-ray/X-ray/infrared fluxes we use these observations as a basis for the theoretical weights. For catalogs with different possible theoretical flux predictions, the sources can be weighted equally to maintain our sensitivity to various signal hypotheses. The spectral index $\gamma$ is assumed to be the same for all sources within a specific stacking search and is a fit parameter along with the total number of signal events $n_s$.

The following is a description of all the searches performed with the 3 yr of IceCube data (similar to those performed in Abbasi et al. 2011b).

*All-sky scan search.* We performed an all-sky search, where the likelihood is evaluated in each direction in the sky in steps of $0°.1 \times 0°.1$ centered at the position of the source $\boldsymbol{x}_s$ over the declination range $-85°$ to $+85°$. In this search the number of effective trials is very high and is related to the number of positions in the grid. The significance of an excess found in some direction needs to be corrected for these trials.

*A list of 44 selected sources.* In order to reduce the large number of effective trials associated with scanning the entire sky, we also performed a search for the most significant of 44 a priori selected source candidates. This source list is selected according to observations in $\gamma$ rays or astrophysical modeling predicting neutrino emission.

*Stacking of six Milagro TeV $\gamma$-ray sources.* This catalog is composed of most of the Milagro sources from Abdo et al. (2007a) considered by Halzen et al. (2008), who estimated their neutrino emission. Four of these sources are in the Cygnus region ($l \in [65°, 85°]$), while two are near a Galactic longitude of $l = 40°$ (Gonzalez-Garcia et al. 2009). The Cygnus region is the brightest extended region in the entire northern sky in TeV $\gamma$ rays (Abdo et al. 2007b). Hadronic models have been postulated to explain the Milagro flux measurements in the Cygnus region (Beacom & Kistler 2007; Anchordoqui et al. 2007, 2009).Given the observation in the IC-40 analysis of a significant a posteriori $p$-value from this catalog, we considered a prescription for future samples, and therefore, the IC-40 data are not used in this analysis to avoid bias. Recent publications by the Milagro collaboration (Abdo et al. 2012) ruled out some of the assumptions about $\gamma$-ray fluxes used in Halzen et al. (2008), so we use an equal weight for each source in the likelihood, with the intention of keeping our sensitivity optimal for all possible signal hypothesis.

*Stacking search for 127 local starburst galaxies.* This search was already performed using IC-40 data (Abbasi et al. 2011b). Starburst galaxies are interesting as possible neutrino sources due to their high star formation rates, especially of high-mass stars (Becker 2008a; Kewley et al. 2001). The large number of stars leads to many SNRs, possibly the sites of CR acceleration below the knee (Hillas 2006). In Becker et al. (2009) the authors associate the far-infrared (FIR) emission with this hot ambient dust and the radio emission with synchrotron losses of electrons, which are assumed to be accelerated along with CRs in the large number of SNRs (Zhang & Fang 2007). The high star formation rate is believed to be the underlying cause for the observed strong correlation between the FIR and the radio flux, and hence, the neutrino fluxes are expected to follow a similar pattern. We perform a stacking search for the catalog of 127 nearby starburst galaxies (Inoue 2011) as compiled in Table A.1 in Becker et al. (2009) using data from Sanders et al. (2003), Moshir et al. (1990), Lisenfeld et al. (2007), and Surace et al. (2004). The high number of sources does not penalize the stacking search because sources are weighted according to their FIR flux at $60\,\mu$m, and therefore, dim sources will contribute less to the likelihood. The highest-weighted starburst galaxy in the catalog is M82 (Lacki et al. 2011), followed by NGC 253 (Romero & Torre 2003).

*Stacking search for five nearby clusters of galaxies.* The stacking search for nearby clusters of galaxies, updated here
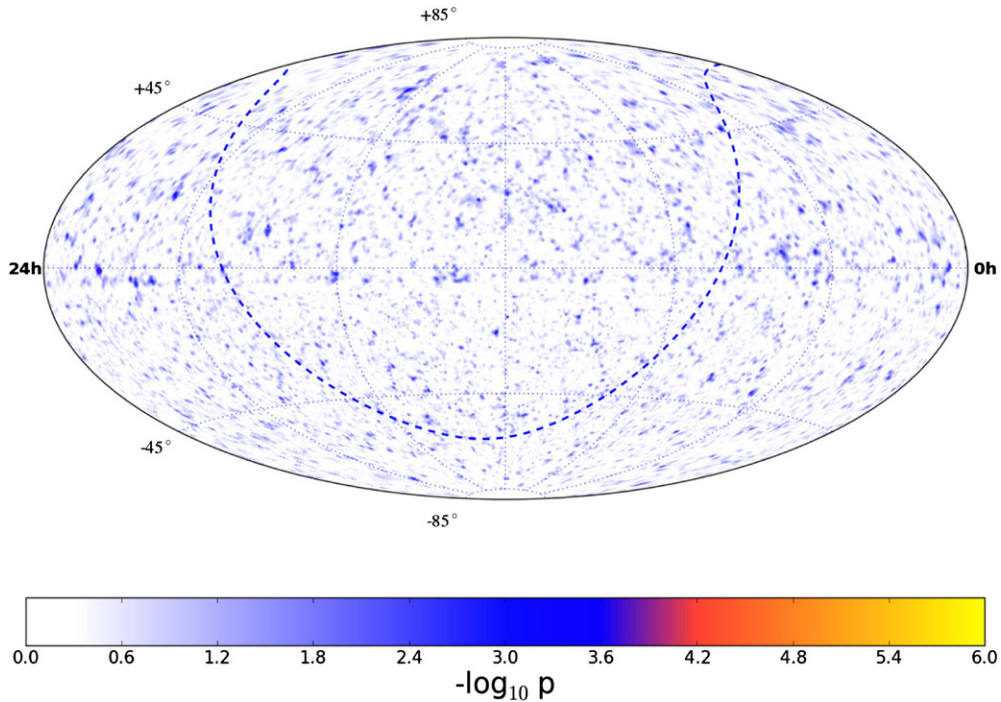
**Figure 12.** Pretrial significance sky map in equatorial coordinates (J2000) of the all-sky point source scan for the combined IC79 + IC59 + IC40 data sample. The dashed line indicates the Galactic plane.

(A color version of this figure is available in the online journal.)

after first results were presented in Abbasi et al. (2011b), is performed by testing four models assuming different CR spatial distributions within the source (Murase et al. 2008). Clusters of galaxies are interesting potential sources of neutrinos that could be produced by interactions between high-energy protons and the intracluster medium (Wolfe et al. 2008). In addition, galaxy clusters are also the largest reservoirs of dark matter, and therefore, it is expected that dark matter self-annihilation could lead to a high luminosity in neutrinos (Murase & Beacom 2013; Dasgupta & Laha 2012). In Murase et al. (2008) the authors discuss four different spectral shapes for the possible neutrino emission from these sources, as characterized by four different models of CR distribution (Pfrommer & Ensslin 2004). The source extensions are different for each model for different sources and are modeled as two-dimensional Gaussian distributions with the corresponding widths for each model. The differential fluxes predicted by Murase et al. (2008) are parameterized as broken power laws as described in Abbasi et al. (2011b) and used as theoretical weights in the likelihood.

*Stacking search for SNRs associated with molecular clouds.* Molecular clouds surrounding SNRs can serve as target for high-energy protons (or heavier nuclei) accelerated by SNR shocks to produce high-energy $\gamma$ rays and neutrinos (Beall 2006). These models predict a high correlation of the expected neutrino flux with the observed $\gamma$-ray emission (Cavasinni et al. 2006). We stack sources from a catalog of close molecular clouds associated with SNRs, which were observed at high energy by *AGILE*, *Fermi*, VERITAS, H.E.S.S., and MAGIC (Abdo et al. 2009a, 2009b, 2010c; Fiasson et al. 2009). Only Galactic sources in the northern sky, where IceCube is sensitive to TeV energies, were selected. The catalog contains four SNRs

associated with molecular clouds: W51C, W44, IC 443, and W49B. The integrated $\gamma$-ray flux above 1 TeV for each source (in Crab units) is used as the theoretical weight in the likelihood. Very recently, the Fermi collaboration detected the characteristic pion decay signature in the $\gamma$-ray emission for two of these SNRs, IC 443 and W44, providing direct evidence that CR protons are accelerated in SNRs (Ackermann et al. 2013) at GeV energies.

*Stacking search for galaxies with supermassive black holes.* Caramete & Biermann (2010) systematically catalogs possible black hole candidates from within the Greisen–Zatsepin–Kuzmin limit (Greisen 1966; Zatsepin & Kuz'min 1966) of around 100 Mpc. In order to keep only the most powerful emitters of particles, a cut of $5 \times 10^8$ solar masses is applied to the catalog to produce a final list of 233 sources. We use as weights the 2 $\mu$m near-infrared flux from the Two Micron All Sky Survey that can be related to the mass of black holes (Caramete & Biermann 2010).

## 5. RESULTS

The results of the all-sky scan are shown in the pretrial significance map of $p$-values in Figure 12. The most significant deviation in the northern sky has a pretrial $p$-value of $1.96 \times 10^{-5}$ and is located at $34°.25$ right ascension and $2°.75$ declination. Similarly, the most significant deviation in the southern sky has a pre-trial $p$-value of $8.97 \times 10^{-5}$ and is located at $219°.25$ right ascension and $-38°.75$ declination.

The posttrial probabilities calculated as the fraction of scrambled sky maps with at least one spot with an equal or higher significance for each hemisphere correspond to 57% and 98% for the northern and the southern spots, respectively, and therefore, both excesses are very compatible with the background
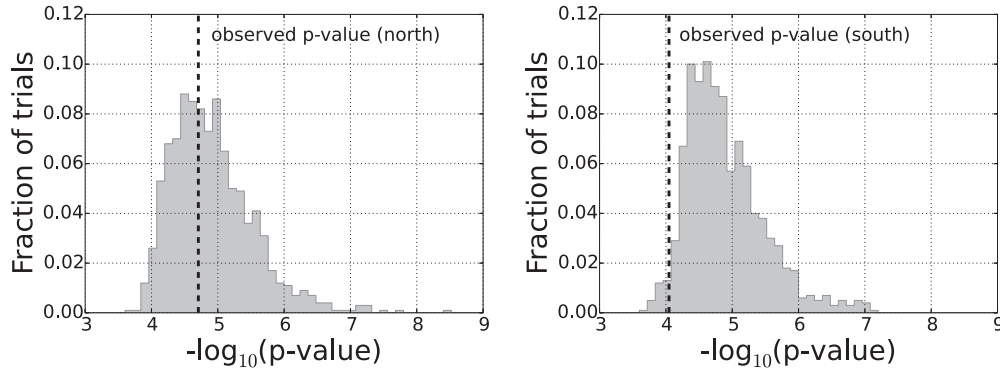
**Figure 13.** Distribution of the smallest *p*-value in (left) the Northern Hemisphere and (right) the Southern Hemisphere, obtained from randomized data. The observed *p*-values of the two hottest spots in the data are indicated by the two dashed vertical lines.

**Table 2**
Results for Galactic Objects on the A Priori Search List

| Category | Source | R.A. (°) | Decl. (°) | *p*-value | $\hat{n}_S$ | $\hat{\gamma}$ | B$_{1°}$ | $\Phi^{90\%}_{\nu_\mu+\bar{\nu}_\mu}$ |
|---|---|---|---|---|---|---|---|---|
| SNR | TYCHO | 6.36 | 64.18 | ... | 0.0 | ... | 11.1 | 3.18 |
| | Cas A | 350.85 | 58.81 | ... | 0.0 | ... | 11.5 | 2.47 |
| | IC443 | 94.18 | 22.53 | 0.43 | 2.8 | 3.9 | 17.2 | 1.63 |
| | MGRO J1908+06 | 286.98 | 6.27 | ... | 0.0 | ... | 23.8 | 1.00 |
| HMXB/mqso | LSI +63 303 | 40.13 | 61.23 | ... | 0.0 | ... | 11.5 | 2.82 |
| | Cyg X-3 | 308.11 | 40.96 | 0.43 | 2.5 | 3.9 | 12.9 | 2.35 |
| | Cyg X-1 | 299.59 | 35.20 | 0.21 | 5.6 | 3.9 | 14.6 | 3.14 |
| | HESS J0632+057 | 98.25 | 5.80 | 0.058[a] | 15.6 | 3.4 | 24.1 | 2.23 |
| | SS433 | 287.96 | 4.98 | ... | 0.0 | ... | 24.3 | 0.92 |
| Star Formation Region | Cyg OB2 | 308.08 | 41.51 | ... | 0.0 | ... | 12.7 | 1.87 |
| Pulsar/PWN | MGRO J2019+37 | 305.22 | 36.83 | ... | 0.0 | ... | 14.3 | 1.83 |
| | Crab Nebula | 83.63 | 22.01 | ... | 0.0 | ... | 17.2 | 1.38 |
| | Geminga | 98.48 | 17.77 | ... | 0.0 | ... | 19.5 | 1.193 |
| Galactic Center | Sgr A* | 266.42 | −29.01 | 0.49 | 0.6 | 3.7 | 25.2 | 13.94 |

**Notes.** Sources are grouped according to their classification as high-mass X-ray binaries or microquasars (HMXB/mqso), SNRs, pulsar wind nebulas (PWNs), and star formation regions. The source MGRO J1908+06 previously considered to be unidentified has been placed in the category of SNR because it is positionally consistent with SNR G40.5−0.5 (Gonzalez-Garcia et al. 2009). The *p*-value is the pretrial probability of compatibility with the background-only hypothesis. The $\hat{n}_S$ and $\hat{\gamma}$ columns give the best fit number of signal events and spectral index of a power law spectrum. When $\hat{n}_S = 0$, no *p*-value or $\hat{\gamma}$ is reported. The eighth column gives the number of background events in a circle of 1° around the search coordinates. The last column shows the upper limits based on the classical approach (Neyman 1937) for an $E^{-2}$ flux normalization of $\nu_\mu + \bar{\nu}_\mu$ flux in units of $10^{-12}$ TeV$^{-1}$ cm$^{-2}$ s$^{-1}$.
[a] Most significant *p*-value in the northern sky among all Galactic and extragalactic objects on the a priori search list.

hypothesis indicating that our data are compatible with only atmospheric muons and neutrinos.

Figure 13 shows the *p*-value distribution for the hottest spot in the Northern Hemisphere (left) and for the Southern Hemisphere (right). The observed *p*-value in the data is indicated in both distributions, and the final posttrial is given by integrating the right-hand side of the distribution from the observed values.

The results of the point source search in the direction of the 44 search selected a priori according to the positions of known objects is summarized in Tables 2 and 3. None of the sources had a significant *p*-value, so we set upper limits for all of them. The smallest *p*-value in the northern sky is found in the direction of HESS J0632+057 with a probability of 5.8%; however, this value is translated into a posttrial probability of 65% once it is compared with an ensemble of randomized sky maps. For the southern sky, the highest significance is observed at the position of PKS 1454−354, with a pretrial *p*-value of 23%,

which corresponds to a posttrial probability of 70%. The fourth column of Tables 2 and 3 shows the upper limits for an $E^{-2}$ flux of $\nu_\mu + \bar{\nu}_\mu$ calculated at a 90% C.L. based on the classical (frequentist) approach (Neyman 1937) for each of the selected objects. The same values are indicated in Figure 14 together with the IceCube sensitivity defined as the median upper limit and the discovery potential. Also shown are the ANTARES upper limits for a list of locations (Adrián-Martínez et al. 2011).

The stacking analysis of the six Milagro TeV sources resulted in a posttrial *p*-value of 20.4% with a best fit $\hat{n}_s = 17$. In the stacking searches of the clusters of galaxies, fewer events than expected from the background were observed for all four models tested, meaning that the *p*-value is at least 50%. Also, the SNRs associated with molecular clouds and the starburst galaxies both resulted in negative fluctuations of the background in every case with $\hat{n}_s = 0$. Finally, the black hole stacking search produced a posttrial *p*-value of 44.3%, with 12 signal events as the best fit.

**Table 3**
Results for Extragalactic Objects on the A Priori Search List

| Category | Source | R.A. (°) | Decl. (°) | $p$-value | $\hat{n}_S$ | $\hat{\gamma}$ | $B_{1°}$ | $\Phi^{90\%}_{\nu_\mu + \bar{\nu}_\mu}$ |
|---|---|---|---|---|---|---|---|---|
| BL Lac | S5 0716+71 | 110.47 | 71.34 | . . . | 0.0 | . . . | 10.3 | 3.60 |
| | 1ES 1959+650 | 300.00 | 65.15 | 0.19 | 5.7 | 3.9 | 11.1 | 5.53 |
| | 1ES 2344+514 | 356.77 | 51.70 | 0.29 | 4.7 | 3.9 | 12.4 | 3.32 |
| | 3C66A | 35.67 | 43.04 | . . . | 0.0 | . . . | 12.7 | 1.86 |
| | H 1426+428 | 217.14 | 42.67 | . . . | 0.0 | . . . | 12.7 | 1.90 |
| | BL Lac | 330.68 | 42.28 | 0.42 | 3.7 | 3.3 | 12.7 | 2.16 |
| | Mrk 501 | 253.47 | 39.76 | 0.34 | 4.8 | 3.9 | 13.4 | 2.84 |
| | Mrk 421 | 166.11 | 38.21 | 0.18 | 3.7 | 1.8 | 13.7 | 3.45 |
| | W Comae | 185.38 | 28.23 | 0.21 | 2.8 | 1.8 | 16.1 | 2.74 |
| | 1ES 0229+200 | 38.20 | 20.29 | 0.19 | 8.2 | 3.9 | 17.8 | 2.43 |
| | PKS 0235+164 | 39.66 | 16.62 | . . . | 0.0 | . . . | 19.9 | 1.30 |
| | PKS 2155−304 | 329.72 | −30.23 | . . . | 0.0 | . . . | 25.5 | 14.28 |
| | PKS 0537−441 | 84.71 | −44.09 | . . . | 0.0 | . . . | 23.8 | 23.27 |
| FSRQ | 4C 38.41 | 248.81 | 38.13 | . . . | 0.0 | . . . | 13.7 | 1.76 |
| | 3C 454.3 | 343.49 | 16.15 | . . . | 0.0 | . . . | 19.9 | 1.23 |
| | PKS 0528+134 | 82.73 | 13.53 | . . . | 0.0 | . . . | 20.8 | 1.14 |
| | PKS 1502+106 | 226.10 | 10.49 | 0.076 | 8.4 | 2.3 | 21.2 | 2.40 |
| | 3C 273 | 187.28 | 2.05 | . . . | 0.0 | . . . | 25.0 | 0.90 |
| | 3C279 | 194.05 | −5.79 | . . . | 0.0 | . . . | 23.5 | 2.06 |
| | QSO 2022−077 | 306.42 | −7.64 | . . . | 0.0 | . . . | 23.2 | 2.47 |
| | PKS 1406−076 | 212.24 | −7.87 | . . . | 0.0 | . . . | 23.2 | 2.49 |
| | QSO 1730−130 | 263.26 | −13.08 | . . . | 0.0 | . . . | 25.6 | 5.04 |
| | PKS 1622−297 | 246.53 | −29.86 | 0.45 | 0.7 | 4.0 | 25.2 | 16.91 |
| | PKS 1454−354 | 224.36 | −35.65 | 0.23[a] | 1.0 | 5.9 | 24.1 | 29.89 |
| Starburst | M82 | 148.97 | 69.68 | . . . | 0.0 | . . . | 10.7 | 4.00 |
| Radio galaxies | NGC 1275 | 49.95 | 41.51 | . . . | 0.0 | . . . | 12.7 | 1.91 |
| | Cyg A | 299.87 | 40.73 | 0.15 | 1.5 | 1.5 | 12.9 | 3.82 |
| | Cen A | 201.37 | −43.02 | 0.46 | 2.0 | 1.4 | 23.9 | 26.62 |
| | 3C 123.0 | 69.27 | 29.67 | . . . | 0.0 | . . . | 15.9 | 1.57 |
| | M87 | 187.71 | 12.39 | 0.45 | 2.9 | . . . | 20.9 | 1.37 |

**Notes.** Sources are grouped according to their classification as BL Lac objects, radio galaxies, flat-spectrum radio quasars (FSRQ), and starburst galaxies. The $p$-value is the pretrial probability of compatibility with the background-only hypothesis. The $\hat{n}_S$ and $\hat{\gamma}$ columns give the best fit number of signal events and spectral index of a power law spectrum. When $\hat{n}_S = 0$, no $p$-value or $\hat{\gamma}$ is reported. The eighth column gives the number of background events in a circle of $1°$ around the search coordinates. The last column shows the upper limits based on the classical approach (Neyman 1937) for an $E^{-2}$ flux normalization of $\nu_\mu + \bar{\nu}_\mu$ flux in units of $10^{-12}$ TeV$^{-1}$ cm$^{-2}$ s$^{-1}$.
[a] Most significant $p$-value in the southern sky among all Galactic and extragalactic objects on the a priori search list.

### 5.1. Implications for Models of Astrophysical Neutrinos

This analysis has not shown evidence of neutrino emission from point sources in the sky. In the absence of a positive detection it is, however, possible to constrain some models that predict astrophysical neutrino emissions. IceCube is entering a new stage in which a nondiscovery has meaningful implications and can provide insight about the nature of these phenomena. IceCube has provided the most constraining upper limits on neutrino fluxes from sources like the Crab Nebulae (Abbasi et al. 2012a). Even though the Crab spectral emission seems to be fully explained by electromagnetic phenomena (Hester 2008), several $\gamma$-ray flares observed in recent years in the GeV region ($E_\gamma > 100$ MeV) challenge purely leptonic models (Abdo et al. 2011). The impact of IceCube limits on different models of neutrino emission from the Crab was already discussed in Abbasi et al. (2012a) for the 40-string configuration of IceCube. Here we update the upper limits based on this 3 yr analysis of IceCube. Figure 15 summarizes a number of different predicted muon neutrino fluxes at Earth according to several models

(standard oscillations have been taken into account). The green solid line corresponds to the flux predicted in Kappes et al. (2007) based on the $\gamma$-ray spectrum measured by H.E.S.S. (Aharonian et al. 2006). As can be seen, the IceCube upper limit is only a factor of two above the flux prediction. This is interesting since it indicates that neutrino astronomy is at the level of sensitivity of $\gamma$-ray astronomy experiments (the factor of two corresponds to the muon neutrino flux lost due to oscillations along the path from the source). The black line represents the estimated flux based on the resonant cyclotron absorption model (Bednarek 2003; Amato et al. 2003). In Amato et al. (2003) inelastic nuclear collisions are considered, and the predicted neutrino rates depend on the pulsar wind Lorentz factor $\Gamma$ of nuclei injected by the pulsar and the effective target density. The predicted flux in Figure 15 is for the most optimistic case of the effective target density and a wind Lorentz factor of $\Gamma = 10^7$, while the favored values of the upstream Lorentz factor of the wind are $\Gamma = 10^6$ (Gallant & Arons 1994). Link & Burgio (2005, 2006) consider scattering of wind protons with the X-ray
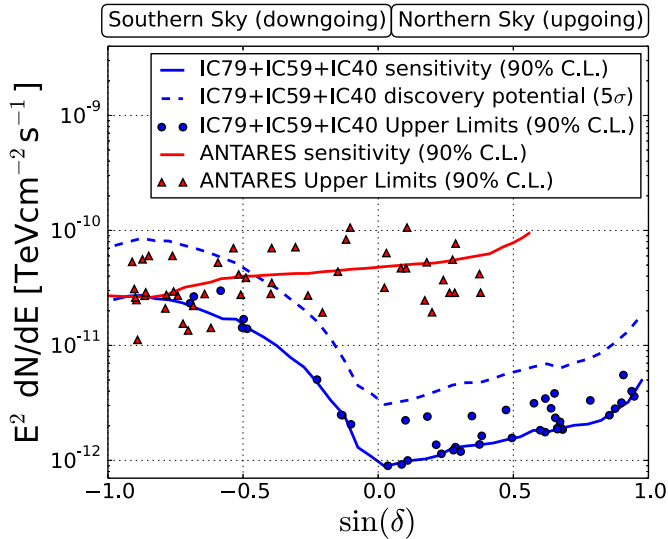
**Figure 14.** Muon neutrino and antineutrino flux 90% C.L. upper limits and sensitivities for an $E^{-2}$ spectrum for an energy range of 1 TeV to 1 PeV in the northern sky and $10^2$ TeV to $10^2$ PeV in the southern sky. Published limits of ANTARES (Adrián-Martínez et al. 2011) are also shown. The different likelihood function and method to derive upper limits used by ANTARES may account for differences in the limits from the two experiments at the level of 20%. In the case of the IceCube method, negative values for the number of signal events are not allowed in the minimization procedure. Therefore, for those sources where there was an underfluctuation of the background, the upper limit matches the median upper limit.

(A color version of this figure is available in the online journal.)
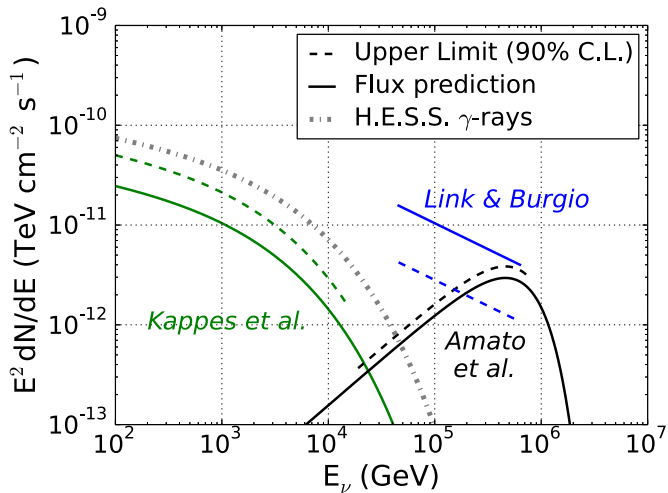


**Figure 15.** Predicted muon neutrino fluxes for several hadronic models for steady neutrino emission from the Crab and upper limits based on 3 yr of IceCube data. Solid lines indicate the flux prediction, and the dashed lines show the corresponding upper limit flux for a 90% C.L. for an energy range that contains 90% of the signal. As a reference, the $\gamma$-ray spectrum measured by H.E.S.S. (Aharonian et al. 2006) is also shown.

(A color version of this figure is available in the online journal.)

emission from the pulsar's surface. The predicted neutrino flux assuming a quadratic scaling of the proton's energy with the height above the surface is shown. The most optimistic version of this model can be rejected with a greater than 90% C.L.

IceCube upper limits are also approaching the predicted neutrino emission from SNRs. In Mandelartz & Becker Tjus (2013) the authors calculate the neutrino spectra generated by proton–proton interactions at SNRs following Kelner et al. (Kelner et al. 2006). In the northern sky, G40.5−0.5 (also known as MGRO J1908+06; Kassim 1989; Yang et al. 2006; Abdo
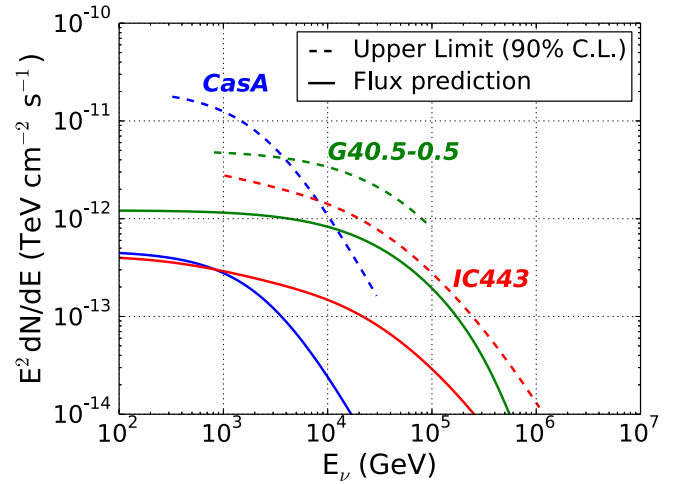


**Figure 16.** Predicted muon neutrino fluxes from three SNRs in the northern sky according to the prediction of Mandelartz & Becker Tjus (2013). The muon neutrino 90% C.L. upper limits from this analysis are shown in the energy range of the 90% signal containment.

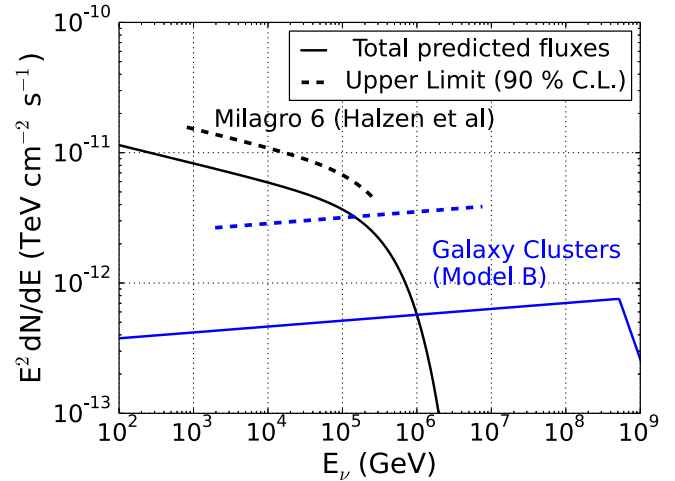(A color version of this figure is available in the online journal.)



**Figure 17.** Predicted muon neutrino fluxes from six Milagro sources in $\gamma$ rays according to Halzen et al. (2008) and from the five nearby galaxy clusters considered in Murase et al. (2008). The corresponding 90% C.L. flux upper limit for muon neutrinos obtained from the stacking analysis is shown as well.

(A color version of this figure is available in the online journal.)

et al. 2007a) seems to be the most promising candidate for neutrino detection due to the high $\gamma$-ray flux observed (Halzen et al. 2008). The measured spectrum is consistent with an $E^{-2}$ dependence from 400 GeV to 40 TeV without evidence of a cutoff (Djannati-Atai et al. 2007). IC443 is also an interesting source with very high energy $\gamma$-ray emission (Albert et al. 2007) and is usually modeled by hadronic interactions (Abdo et al. 2010b; Li & Chen 2012). It was observed in the upper TeV by Milagro with a significance of $3\sigma$ (Abdo et al. 2009b).

Figure 16 shows the predicted muon neutrino spectra after considering oscillations for these two SNRs and Cas A (Hwang & Laming 2012; Araya & Cui 2010; Abdo et al. 2010a). The 90% C.L. flux upper limit for muon neutrinos is also shown.

As can be seen, IceCube upper limits in the most optimistic case, for G40-5.0.5, are still a factor of four above the flux prediction. However, stacking techniques can improve the discovery potential.

Figure 17 shows the upper limit of the stacking result of the six Milagro TeV $\gamma$-ray associations assuming the model from

Halzen et al. (2008). The result of the analysis was a positive fluctuation, so the sensitivity is expected to be closer to the total predicted flux than the upper limit. Together in Figure 17 we show the flux prediction and the corresponding upper limit from the search for five nearby galaxy clusters assuming that CRs are uniformly distributed within the virial radius of the galaxy cluster.

## 6. SYSTEMATIC UNCERTAINTIES

One of the strengths of the presented searches is that they use a background estimation based on randomized data. The $p$-values are unaffected by uncertainties in the theoretical estimate of fluxes of the background of atmospheric neutrinos and muons that depend on hadronic models of shower development in the atmosphere and on the CR composition. They are also unaffected by the poorly known contribution of prompt neutrinos. Moreover, uncertainties in the simulation of the detector also do not affect the posttrial $p$-value.

However, the construction of the signal energy density function in the likelihood method depends on the simulation and is therefore affected by the systematic uncertainties. Hence, the upper limits derived from the nonobservation of neutrinos depend on these systematic effects as well. In order to capture the impact of the systematic uncertainties, we fully propagated each of them through the likelihood search and calculated the sensitivity of the search for a discrete set of simulated signal responses within the allowed range of uncertainties. We used the IC-79 data sample for this evaluation, and we quote the declination-averaged uncertainties under the assumption that all samples are affected by the same systematic errors. This assumption can be regarded as conservative since the lower-energy range is more strongly affected by the uncertainties and the IC-79 sample contains the largest number of low-energy events.

The two most relevant uncertainties come from the absolute efficiency of the optical modules and the modeling of the optical properties of the ice. As a conservative estimate, we allowed for a $\pm 10\%$ uncertainty in the absolute efficiency of the optical modules. Uncertainties in the relative sensitivity of the individual DOMs with respect to the detector average have been observed to have a negligible impact on the total flux uncertainty in the energy range of this analysis. Likewise, there is no significant impact if the sensitivity of the high-quantum-efficiency PMTs in DeepCore (Abbasi et al. 2012b) is larger with respect to the rest of the detector. This is due to the limited size of this part of the detector with respect to the typical track length of the events selected in this analysis. The uncertainty of $\pm 10\%$ in DOM efficiency in the simulation resulted in $+6\%/-7\%$ variation in the sensitivity of IC-79. The parameterization of the optical properties of the ice used in this work is a variant of the parameterization presented in (Abbasi et al. 2013c). Its uncertainties have been taken to be $\pm 10\%$ in absorption and scattering, and they both have been rescaled at the same time. The effect on the sensitivity coming from these variations was $+5\%/-8\%$.

Due to constraints in computing power, we used tabulated photon arrival probabilities in the signal simulation (Lundberg et al. 2007). A more accurate description of the detector response can be obtained by using a simulation with direct photon propagation (Chirkin et al. 2013). The difference between the two methods is most relevant for energies below $\sim 1$ TeV and decreases with energy. In order to quantify the impact of the photon propagation method, we compared the difference in sensitivity in the northern sky using simulated data generated specifically for this purpose. The impact on the Southern Hemisphere is expected to be smaller, and the values for the northern sky thus represent a conservative estimate for the full sky. The difference in sensitivity, 7.2%, between the two propagators can be accounted for by the uncertainty in the optical efficiency and therefore is not considered here as an additional source of systematic uncertainty. Future simulations of IceCube are expected to be produced with direct photon propagation, and an increase in the nominal optical efficiency of 10% is also foreseen since a higher optical efficiency was found to better describe IceCube data.

There is a small probability that southern sky signal neutrinos are vetoed by the IceTop veto applied in the IC-79 and IC-59 data samples due to random coincidences. As can be seen in Figure 4 (left), this probability for random coincidences is constantly below 1% at all declinations and can therefore be neglected compared to the impact of other systematic uncertainties.

By summing in quadrature all the different contributions, the expected uncertainty in the IC-79 sensitivity is about 18%. This is compatible with the 16% estimated for the IC-40 configuration (Abbasi et al. 2011b).

The upper limits listed in the previous section have been calculated for a pure muon neutrino signal under the assumption that no other neutrino flavors contribute in this analysis. Considering neutrino oscillations with a large mixing angle $\Theta_{23} \sim 45°$ and a long baseline, a typical neutrino flavor ratio of $\nu_e : \nu_\mu : \nu_\tau = 1:2:0$ at the source will result in an approximate partition of 1:1:1 at Earth. In the case of $\nu_\tau$ the resulting $\tau$ will decay into a $\mu$ with a branching ratio of about 17%. These additional muons from $\nu_\tau$ can contribute to a possible signal flux in this analysis. In Abbasi et al. (2011b), the contribution of $\nu_\tau$ in addition to the $\nu_\mu$ flux simulated in this work has been determined to be 10%–16% of the $\nu_\mu$ contribution.

## 7. CONCLUSIONS

We present the results of the point source analysis of 3 yr of data with the 40-string, 59-string, and 79-string configurations of the IceCube Neutrino Observatory. The combined data have a total live-time of 1040 days from 2008 April to 2011 May. The all-sky survey found no evidence of point source neutrino emission in the Northern Hemisphere or the Southern Hemisphere. The posttrial probabilities of the highest significant coordinate in each hemisphere are compatible with background fluctuations. Additionally, a search on a catalog of known emitters of high-energy radiation was performed. Several stacking analyses were carried out to integrate the possible signal from all sources of the same class. Also, in this case, no significant deviation from the background hypothesis was found, and the corresponding 90% C.L. upper limits on the muon neutrino fluxes were calculated and compared to predictions. The most optimistic models considered here can be excluded at the 90% C.L., and in other cases limits are a factor of two to four above the predictions.

The muon neutrino upper limits presented here improve earlier results (Abbasi et al. 2011b) by a factor $\sim 3.5$ or better and are the strictest neutrino limits to date over the entire sky. Some of these limits for an $E^{-2}$ muon neutrino flux have reached the level of $10^{-12}$ TeV cm$^{-2}$ s$^{-1}$ necessary to test current models of neutrino emission expected for Galactic sources like SNRs (Vissani et al. 2011; Yuan et al. 2011). In the future, the sensitivity of IceCube to a neutrino point source will improve with the inclusion of additional data collected with the full IceCube array.

**Table 4**
Muon Neutrino Effective Areas

| $\log_{10} E_{min}$ | $\log_{10} E_{max}$ | North ($0° < \delta \leqslant 90°$) | | | South ($-90° \leqslant \delta \leqslant 0°$) | | |
|---|---|---|---|---|---|---|---|
| | | IC-79 | IC-59 | IC-40 | IC-79 | IC-59 | IC-40 |
| 3.00 | 3.25 | 0.41 | 0.28 | 0.12 | 0.02 | 0.01 | 0.00 |
| 3.25 | 3.50 | 1.11 | 0.78 | 0.34 | 0.06 | 0.04 | 0.01 |
| 3.50 | 3.75 | 2.65 | 2.01 | 1.07 | 0.17 | 0.11 | 0.04 |
| 3.75 | 4.00 | 5.87 | 4.65 | 2.56 | 0.46 | 0.32 | 0.11 |
| 4.00 | 4.25 | 11.83 | 9.58 | 5.52 | 1.05 | 0.78 | 0.34 |
| 4.25 | 4.50 | 21.77 | 18.36 | 12.00 | 2.52 | 1.83 | 0.74 |
| 4.50 | 4.75 | 36.99 | 31.67 | 22.86 | 5.36 | 3.74 | 1.83 |
| 4.75 | 5.00 | 58.47 | 50.86 | 34.85 | 10.88 | 7.99 | 3.26 |
| 5.00 | 5.25 | 87.14 | 76.92 | 55.80 | 21.77 | 15.87 | 7.87 |
| 5.25 | 5.50 | 121.76 | 108.50 | 81.50 | 42.85 | 30.24 | 15.34 |
| 5.50 | 5.75 | 160.62 | 144.95 | 110.00 | 80.52 | 57.23 | 27.82 |
| 5.75 | 6.00 | 205.52 | 187.38 | 141.89 | 147.57 | 106.95 | 53.59 |
| 6.00 | 6.25 | 251.32 | 228.80 | 181.35 | 237.05 | 175.87 | 95.41 |
| 6.25 | 6.50 | 300.92 | 280.14 | 216.07 | 360.95 | 275.64 | 172.67 |
| 6.50 | 6.75 | 349.98 | 335.04 | 270.26 | 511.18 | 402.76 | 251.98 |
| 6.75 | 7.00 | 406.74 | 379.00 | 298.75 | 701.98 | 549.56 | 366.78 |
| 7.00 | 7.25 | 452.88 | 440.70 | 358.44 | 949.45 | 759.58 | 498.23 |
| 7.25 | 7.50 | 497.98 | 481.35 | 419.92 | 1248.55 | 999.85 | 649.27 |
| 7.50 | 7.75 | 561.75 | 531.64 | 482.86 | 1623.10 | 1324.28 | 834.44 |
| 7.75 | 8.00 | 603.41 | 596.59 | 488.16 | 2084.37 | 1709.82 | 993.06 |
| 8.00 | 8.25 | 660.84 | 660.13 | 535.53 | 2642.73 | 2164.94 | 1297.21 |
| 8.25 | 8.50 | 719.94 | 732.64 | 520.84 | 3353.95 | 2779.39 | 1453.31 |
| 8.50 | 8.75 | 774.93 | 780.96 | 648.86 | 4227.17 | 3443.88 | 1608.56 |
| 8.75 | 9.00 | 813.21 | 839.18 | 632.89 | 5307.43 | 4261.46 | 1746.93 |

**Notes.** Solid-angle-averaged neutrino effective area for $\nu_\mu + \bar{\nu}_\mu$ in the north and south skies. The first two columns indicate the limits of the energy bin so that $\log_{10}[E_{min}] < \log_{10}[E_\nu (\text{GeV})] \leqslant \log_{10}[E_{max}]$. The muon neutrino effective area is shown in units of m$^2$ for each of the three configurations.

## APPENDIX

### MUON NEUTRINO EFFECTIVE AREA

Table 4 presents the tabulated values of the solid-angle-averaged muon neutrino effective for the three different configurations used in this analysis.

## REFERENCES

Abbasi, R., Ackermann, M., Adams, J., et al. (IceCube Collaboration) 2009a, NIMPA, 601, 294
Abbasi, R., Abdou, Y., Abu-Zayyad, T., et al. (IceCube Collaboration) 2009b, PhRvL, 103, 221102
Abbasi, R., Abdou, Y., Abu-Zayyad, T., et al. (IceCube Collaboration) 2010, NIMPA, 618, 139
Abbasi, R., Abdou, Y., Abu-Zayyad, T., et al. (IceCube Collaboration) 2011a, PhRvD, 83, 012001
Abbasi, R., Abdou, Y., Abu-Zayyad, T., et al. (IceCube Collaboration) 2011b, ApJ, 732, 18
Abbasi, R., Abdou, Y., Abu-Zayyad, T., et al. (IceCube Collaboration) 2012a, ApJ, 745, 45
Abbasi, R., Abdou, Y., Abu-Zayyad, T., et al. (IceCube Collaboration) 2012b, APh, 35, 615
Abbasi, R., Abdou, Y., Ackermann, M., et al. (IceCube Collaboration) 2013a, ApJ, 763, 33
Abbasi, R., Abdou, Y., Ackermann, M., et al. (IceCube Collaboration) 2013b, NIMPA, 700, 188
Abbasi, R., Abdou, Y., Ackermann, M., et al. (IceCube Collaboration) 2013c, NIMPA, 711, 73
Abbasi, R., Abdou, Y., Ackermann, M., et al. (IceCube Collaboration) 2013d, NIMPA, 703, 190
Abdo, A. A., Abeysekara, U., Allen, B. T., et al. 2012, ApJ, 753, 159
Abdo, A. A., Ackermann, M., Ajello, M., et al. (Fermi Collaboration) 2009a, ApJL, 706, L1
Abdo, A. A., Ackermann, M., Ajello, M., et al. (Milagro Collaboration) 2010a, ApJL, 710, L92
Abdo, A. A., Ackermann, M., Ajello, M., et al. (Milagro Collaboration) 2010b, ApJ, 712, 459
Abdo, A. A., Ackermann, M., Ajello, M., et al. (Fermi Collaboration) 2010c, Sci, 327, 1103
Abdo, A. A., Ackermann, M., Ajello, M., et al. (Fermi Collaboration) 2011, Sci, 331, 739
Abdo, A. A., Allen, B., Berley, D., et al. (Milagro Collaboration) 2007a, ApJL, 664, L91
Abdo, A. A., Allen, B., Berley, D., et al. (Milagro Collaboration) 2007b, ApJL, 658, L33

Abdo, A. A., Allen, B. T., Aune, T., et al. (Milagro Collaboration) 2009b, ApJL, 700, L127

Achterberg, A., Ackermann, M., Adams, J., et al. 2006, APh, 26, 282

Ackermann, M., Ajello, M., Allafort, A., et al. (Fermi Collaboration) 2013, Sci, 339, 807

Adrián-Martínez, S., Aguilar, J. A., Samarai, I. A., et al. (ANTARES Collaboration) 2011, ApJL, 743, L14

Aharonian, F., Akhperjanian, A. G., Bazer-Bachi, A. R., et al. (HESS Collaboration) 2006, A&A, 457, 899

Ahrens, J., Bai, X., Bay, R., et al. (AMANDA Collaboration) 2004, NIMPA, 524, 169

Albert, J., Aliu, E., Anderhub, H., et al. (MAGIC Collaboration) 2007, ApJL, 664, L87

Amato, E., Guetta, D., & Blasi, P. 2003, A&A, 402, 827

Anchordoqui, L. A., Beacom, J. F., Goldberg, H., Palomares-Ruiz, S., & Weiler, T. J. 2007, PhRvD, 75, 063001

Anchordoqui, L. A., Goldberg, H., Moore, R. D., et al. 2009, PhRvD, 80, 103004

Anchordoqui, L. A., & Montaruli, T. 2010, ARNPS, 60, 129

Araya, M., & Cui, W. 2010, ApJ, 720, 20

Auffenberg, J., et al. (IceCube Collaboration) 2011, in Proc. of the 32nd Int. Cosmic Ray Conf., Beijing, China (arXiv:1111.2736)

Beacom, J. F., & Kistler, M. D. 2007, PhRvD, 75, 083001

Beall, J. H. 2006, ChJAA, 6, 147

Becker, J. 2008a, PhR, 458, 173

Becker, J. K. 2008b, PhR, 458, 173

Becker, J., Biermann, P. L., Dreyer, J., & Kneiske, T. M. 2009, arXiv:0901.1775

Bednarek, W. 2003, A&A, 407, 1

Bell, A. R. 1978, MNRAS, 182, 147

Braun, J., Baker, M., Dumm, J., et al. 2010, APh, 33, 175

Caramete, L., & Biermann, P. L. 2010, A&A, 521, A55

Cavasinni, V., Grasso, D., & Maccione, L. 2006, APh, 26, 41

Chirkin, D., et al. (IceCube Collaboration) 2013, NIMPA, 725, 141

Dasgupta, B., & Laha, R. 2012, PhRvD, 86, 093001

Dermer, C. D., & Powale, G. 2013, A&A, A34, 553

Desiati, P., et al. (IceCube Collaboration) 2011, in Proc. of the 32nd Int. Cosmic Ray Conf., Beijing, China (arXiv:1111.2735)

Djannati-Atai, A., Ona-Wilhelmi, E., Renaud, M., et al. (H.E.S.S. Collaboration) 2007, in Proc. of the 30th Int. Cosmic Ray Conf., Merida, Mexico (arXiv:0710.2418)

Fiasson, A., et al. (HESS Collaboration) 2009, in Proc. of the 31st Int. Cosmic Ray Conf., Lodz, Poland

Gallant, Y. A., & Arons, J. 1994, ApJ, 435, 230

Gonzalez-Garcia, M. C., Halzen, F., & Mohapatra, S. 2009, APh, 31, 437

Greisen, K. 1966, PhRvL, 16, 748

Halzen, F., Kappes, A., & O'Murchadha, A. 2008, PhRvD, 78, 063004

Hastie, T., Tibshirani, R., & Friedman, J. H. 2009, The Elements of Statistical Learning: Data Mining, Inference, and Prediction (New York: Springer)

Hester, J. J. 2008, ARA&A, 46, 127

Hillas, A. M. 2006, JPhCS, 47, 168

Honda, M., Kajita, T., Kasahara, K., Midorikawa, S., & Sanuki, T. 2007, PhRvD, 75, 043006

Hwang, U., & Laming, J. M. 2012, ApJ, 746, 130

Inoue, Y. 2011, ApJ, 728, 11

Kappes, A., Hinton, J., Stegmann, C., & Aharonian, F. A. 2007, ApJ, 656, 870

Kassim, N. E. 1989, ApJS, 71, 799

Kelner, S. R., Aharonian, F., & Bugayov, V. V. 2006, PhRvD, 74, 034018

Kerthi, S. S., Shevade, S. K., Bhattacharyya, C., et al. 2001, Neural Comput., 13, 637

Kewley, L. J., Dopita, M. A., Sutherland, R. S., Heisler, C. A., & Trevena, J. 2001, ApJ, 556, 121

Kistler, M. D., & Beacom, J. F. 2006, PhRvD, 74, 063007

Lacki, B. C., Thompson, T. A., Quataert, E., Loeb, A., & Waxman, E. 2011, ApJ, 734, 107

Learned, J. G., & Mannheim, K. 2000, ARNPS, 50, 679

Li, H., & Chen, Y. 2012, MNRAS, 421, 935

Link, B., & Burgio, F. 2005, PhRvL, 94, 181101

Link, B., & Burgio, F. 2006, MNRAS, 371, 375

Lisenfeld, U., Verdes-Montenegro, L., Sulentic, J., et al. 2007, A&A, 462, 507

Lundberg, J., Miočinović, P., Woschnagg, K., et al. 2007, NIMPA, 581, 619

Mandelartz, M., & Becker Tjus, J. 2013, ApJ, submitted (arXiv:1301.2437)

Masbou, J., et al. (HESS Collaboration) 2009, in Proc. of the 31st Int. Cosmic Ray Conf., Lodz, Poland

Moshir, M., Kopan, G., Conrow, T., et al. 1990, BAAS, 22, 1325

Murase, K., & Beacom, J. F. 2013, JCAP, 1302, 028

Murase, K., Inoue, S., Nagataki, S., et al. 2008, ApJL, 689, L105

Neyman, J. 1937, RSPTA, 236, 333

Pfrommer, C., & Ensslin, T. A. 2004, A&A, 426, 777

Romero, G. E., & Torre, D. F. 2003, ApJL, 586, L33

Sanders, D. B., Mazzarella, J. M., Kim, D.-C., Surace, J. A., & Soifer, B. T. 2003, AJ, 126, 1607

Schlickeiser, R. 1989, ApJ, 336, 243

Surace, J. A., Sanders, D. B., & Mazzarella, J. M. 2004, AJ, 127, 3235

Vissani, F. 2006, APh, 26, 310

Vissani, F., Aharonian, F., & Sahakyan, N. 2011, APh, 34, 778

Wolfe, B., Melia, F., Crocker, R. M., & Volkas, R. R. 2008, ApJ, 687, 193

Yang, J., Zhang, J.-L., Cai, Z.-Y., Lu, D.-R., & Tan, Y.-H. 2006, ChJAA, 6, 210

Yuan, Q., Yin, P.-F., & Bin, X.-J. 2011, APh, 35, 33

Zatsepin, G. T., & Kuz'min, V. A. 1966, JETPL, 4, 78

Zhang, L., & Fang, J. 2007, ApJ, 666, 247